

## DIPLOMARBEIT

# Validation of the AllPix<sup>2</sup> simulation framework for the development of SiC particle detectors

im Rahmen des Studiums  
**Technische Physik**

eingereicht von  
**Paul Sommerer**  
Matrikelnummer: 01608032

ausgeführt am  
Atominstitut der TU Wien und am  
Institut für Hochenergiephysik der Österreichischen Akademie der Wissenschaften

Betreuung:  
Assistant Prof. DI Dr.techn. Albert Hirtl (TU Wien / Atominstitut)  
DI Dr.techn. Thomas Bergauer (ÖAW / HEPHY)

Wien, 18. Januar 2024

---

(Unterschrift Verfasser)

---

(Unterschrift Betreuer)

## Abstract

In this thesis, the viability of the Monte Carlo simulation framework AllPix<sup>2</sup> for the development of silicon carbide (SiC) based particle detectors is explored. A new set of parameters for the Jacoboni Canali charge carrier mobility model, suitable for the simulation of SiC, is introduced. A workflow for running AllPix<sup>2</sup> simulations with field data obtained from simulations using the Synopsys TCAD simulation suite is demonstrated. Using this setup, real world experiments on a prototype 4H-SiC detector are compared to the results from corresponding AllPix<sup>2</sup> simulations.

The evaluated parameters include the charge collection efficiency (CCE) for three different types of radiation, UV-laser, proton and alpha particle, as well as the timing performance of the SiC detector using a UV-laser.

Comparison of the experiment data to the results of the corresponding AllPix<sup>2</sup> simulations shows very close agreement on CCE. The timing performance of the simulation setups is however larger than that observed in the real world experiment.

## Zusammenfassung

In dieser Arbeit wird die Realisierbarkeit von Simulationen mit dem Monte-Carlo Simulationsprogramm AllPix<sup>2</sup> für die Entwicklung neuer Silizium-Karbid (SiC) Teilchendetektoren erforscht. Ein neuer, für die Simulation von SiC geeigneter Parametersatz für das Jacoboni-Canali Mobilitätsmodell wird eingeführt, sowie ein Workflow für die Durchführung von AllPix<sup>2</sup> Simulationen mit Felddaten, die aus Simulationen mit der TCAD Simulations-Suite Synopsys stammen, vorgestellt. Unter diesen Voraussetzungen werden Experimente an einem Prototyp-Detektor auf 4H-SiC-Basis mit den Ergebnissen entsprechender AllPix<sup>2</sup> Simulationen verglichen.

Die verglichenen Größen beinhalten die Charge Collection Efficiency (CCE) für drei verschiedene Arten von Strahlung, UV-Laser, Proton und Alpha-Partikel, sowie die Timing-Leistung des SiC-Detektors unter Verwendung eines UV-Lasers.

Der Vergleich der Experimentdaten mit den Ergebnissen der entsprechenden AllPix<sup>2</sup> Simulationen zeigt sehr gute Übereinstimmung für die CCE. Die Timing-Leistung der Simulation ist jedoch besser als jene, die für das Experiment beobachtet wird.

## Acronyms

**AC** alternating current.

**CCE** charge collection efficiency.

**CFD** constant fraction discriminator.

**CSA** charge sensitive amplifier.

**FWHM** full width half maximum.

**GPS** general particle source.

**HEPHY** institute of high energy physics.

**MIP** minimum ionizing particle.

**RMS** root mean square.

**SiC** silicon carbide.

**TCAD** technology computer aided design.

**TIA** transimpedance amplifier.

**UCSC** university of Santa Cruz.

# Contents

<b>1. Introduction</b>	<b>7</b>
<b>2. Physical and Technical Background</b>	<b>8</b>
2.1. Interactions of Radiation with Matter . . . . .	8
2.1.1. Ion radiation . . . . .	8
2.1.2. Photon radiation . . . . .	11
2.2. Semiconductors and Detectors . . . . .	12
2.2.1. Semiconductors . . . . .	12
2.2.2. Diode . . . . .	13
2.2.3. Semiconductor Detectors . . . . .	13
2.2.4. Signal Formation - Shockley-Ramo Theorem . . . . .	14
2.2.5. Signal Fluctuation and Fano Factor . . . . .	15
2.2.6. Signal Timing . . . . .	16
2.3. Silicon Carbide . . . . .	18
<b>3. Materials and Methods</b>	<b>19</b>
3.1. AllPix <sup>2</sup> . . . . .	19
3.1.1. Deposition . . . . .	19
3.1.2. Propagation . . . . .	20
3.1.3. PulseTransfer . . . . .	24
3.1.4. CSADigitizer . . . . .	24
3.1.5. ROOTObjectWriter . . . . .	25
3.2. Pulse Analyzer . . . . .	25
3.2.1. Time Resolution Measurement . . . . .	25
3.2.2. Charge Collection Efficiency . . . . .	26
3.3. Detector Prototype . . . . .	27
3.4. Readout Electronics . . . . .	29
3.4.1. UCSCSingleChannel Amplifier . . . . .	29
3.4.2. Cividec Cx-L . . . . .	30
3.5. TCAD Fields . . . . .	30
3.5.1. Workflow . . . . .	30
3.6. Simulation Workflow . . . . .	34
3.6.1. HTCondor . . . . .	34
3.6.2. Docker . . . . .	34
3.6.3. Simluation Scans . . . . .	35
3.7. Experimental Setups . . . . .	36
3.7.1. UV-Laser Experiments . . . . .	36
3.7.2. Proton Experiments . . . . .	38
3.7.3. Alpha Experiments . . . . .	39

<b>4. Results</b>	<b>41</b>
4.1. UV-Laser Simulations . . . . .	41
4.1.1. Charge Collection Efficiency . . . . .	41
4.1.2. Pulse Shape Comparison . . . . .	43
4.1.3. Time Resolution . . . . .	46
4.2. Proton Simulations . . . . .	47
4.2.1. Charge Collection Efficiency . . . . .	49
4.3. Alpha Simulations . . . . .	50
4.3.1. Charge Collection Efficiency . . . . .	50
<b>5. Conclusion</b>	<b>53</b>
<b>References</b>	<b>55</b>
<b>A. Appendix</b>	<b>62</b>
A.1. Configuration of the Transient-TCAD UV-Laser Simulation . . . . .	62
A.2. Python Code for Weighting Field Calculation . . . . .	65
A.3. Python Code for AllPix <sup>2</sup> ROOT File Analysis . . . . .	66

Die approbierte gedruckte Originalversion dieser Diplomarbeit ist an der TU Wien Bibliothek verfügbar  
 The approved original version of this thesis is available in print at TU Wien Bibliothek.

# 1. Introduction

In recent years, the production quality of silicon carbide (SiC) wafers has increased, mostly due to the increased demand from applications in the power electronics industry. SiC is replacing conventional silicon as the material of choice in high-efficiency, high-frequency and high-temperature applications, such as the electric vehicle market, including the charging infrastructure, and the photovoltaic sector [1]. Compared to silicon, SiC based designs can feature much improved switching frequencies, resulting in increased efficiency and more compact designs [2].

Due to its physical properties, the material could however also find application as a detector material, more specifically in the field of high energy physics, where it could also replace the well established silicon. Silicon carbide is a high bandgap material, significantly reducing leakage currents at room temperature, even after irradiation, which, in combination with its higher thermal conductivity, greatly facilitates temperature control of the detector. Its higher atomic displacement energy implies greater radiation hardness, which could enable applications in extreme environments. Another beneficial characteristic is its higher saturated charge carrier velocity, improving the theoretically obtainable time resolution. The electric fields needed to reach said saturation velocities can easily be reached due to the high breakdown fields of silicon carbide.

As with any new development, accurate and reliable computer simulations of the underlying processes are imperative, to reduce the number of time and cost intensive design iterations. The Monte Carlo simulation framework AllPix<sup>2</sup> is a well established candidate for the simulation of particle detectors, however it was developed with silicon detectors in mind. The necessary adaptation of AllPix<sup>2</sup> to support silicon carbide as a detector material is made possible by its open-source mentality and excellent documentation. Cooperation with external TCAD simulation tools is enabled by its support for common file types.

In the scope of this thesis, the capabilities of AllPix<sup>2</sup> with respect to the accurate simulation of SiC are investigated, by comparing the results of real-world experiments on a prototype SiC detector with the results of the corresponding simulations.

## 2. Physical and Technical Background

### 2.1. Interactions of Radiation with Matter

Different types of radiation have different characteristics in their interaction with matter. The two radiation types used in the scope of this thesis, photon and ion, are described in this section.

#### 2.1.1. Ion radiation

##### Inelastic Scattering at the Shell Electrons

When a charged particle traverses a material, it can scatter at the material's shell electrons, passing off some of its kinetic energy. Since the amount of energy transmitted is relatively small, the path of the particle does not experience significant changes. However, as the charged particle encounters numerous such interactions while passing through the material, this effect becomes the primary contributor to the overall energy loss for particles with low energies.

##### Multiple Coulomb Scattering at the Atomic Nuclei

In addition, charged particles have the potential to undergo scattering within the electromagnetic field of the atomic nuclei. When the mass of the incoming particle is significantly smaller than that of the material's nuclei, this scattering process is elastic, meaning it only alters the direction of the particle's path. If the particle scatters at multiple nuclei as it traverses the material, the resulting scattering angle can no longer be predicted using Rutherford's equation. Instead, it follows a Gaussian distribution, as explained by Molière [3].

##### Energy Deposition - Bethe Bloch Equation and Landau Distribution

The quasi-continuous energy loss of charged particles traversing a material is described by the Bethe-Bloch equation [4]

$$\left\langle -\frac{dE}{dx} \right\rangle = 4\pi N_A r_e^2 c^2 \rho^2 \frac{Z}{A} \frac{z^2}{\beta^2} \left[ \frac{1}{2} \ln \frac{2m_e c^2 \beta^2 \gamma^2 W_{\max}}{I^2} - \beta^2 - \frac{\delta(\beta\gamma)}{2} \right], \quad (2.1)$$

with the parameters in Table 2.1. The quotient  $\left\langle -\frac{dE}{dx} \right\rangle$  is called linear stopping power.

Symbol	Description	Value or unit
$N_A$	Avogadro's constant	$6.022 \times 10^{23} \text{ mol}^{-1}$
$r_e$	Classical electron radius	2.818 fm
$c$	Speed of light	$299\,792\,458 \text{ m s}^{-1}$
$\rho$	Density	$\text{g cm}^{-3}$
$z$	Charge number of incident particle	$e$
$Z$	Atomic number of absorber	
$A$	Atomic mass of absorber	$\text{g mol}^{-1}$
$W_{\text{max}}$	Maximum energy transfer in a single collision	MeV
$I$	Mean excitation potential	eV
$\beta$	$v/c$	
$\gamma$	$\frac{1}{\sqrt{1-\beta^2}}$	
$\delta(\beta\gamma)$	Density correction	

**Table 2.1:** Bethe-Bloch equation parameters.

Figure 2.1 shows a plot of the equation for different materials. In this figure, a shared minimum of the mean energy transfer at an impulse to mass ratio  $\beta\gamma = \frac{p}{mc} \approx 3$  can be seen. Particles at these respective velocities are called minimum ionizing particle (MIP). MIPs play a special role in high energy physics, as they dictate the required energy resolution for a detector.

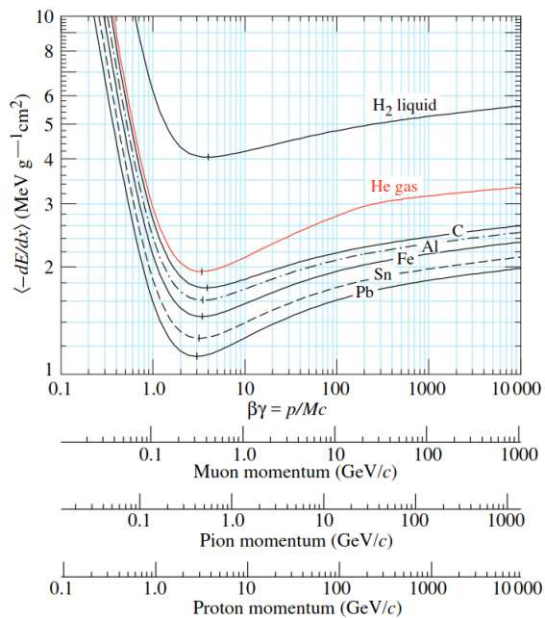


**Figure 2.1:** Bethe-Bloch equation for a number of different materials. [4]

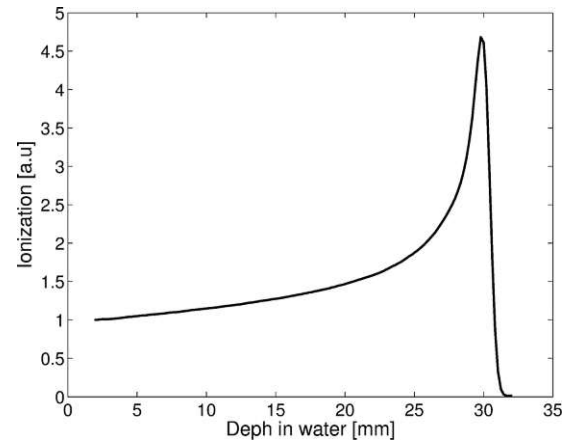


**Figure 2.2:** Bragg peak exhibited by 62 MeV protons in water [5].

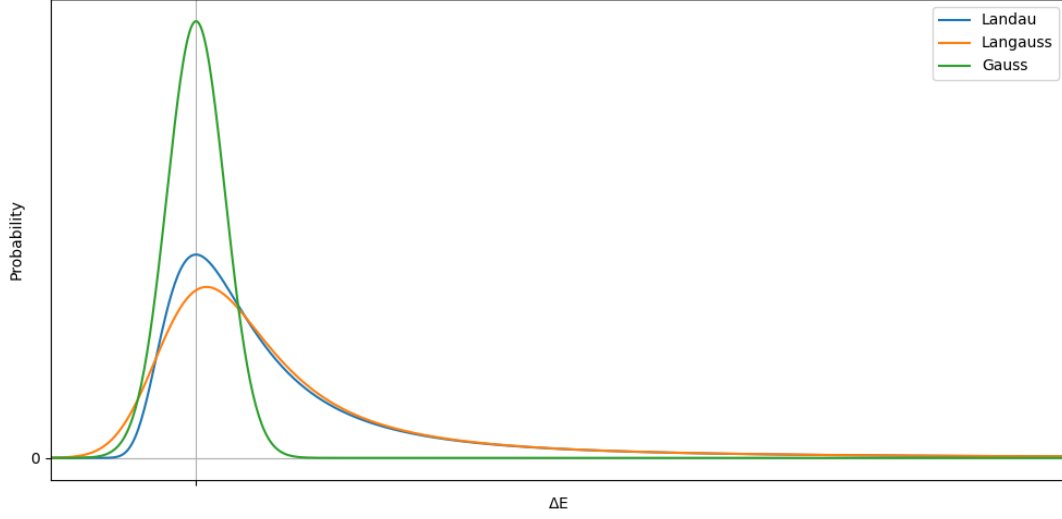


**Figure 2.3:** Comparison between the symmetric Gauss distribution and the asymmetric Landau and Langau distributions.

Due to the  $\frac{1}{\beta^2}$  factor in equation 2.1, a particle deposits most of its energy towards the end of its trajectory before coming to a complete stop. This behavior results in the so-called Bragg peak in the stopping power versus penetration depth plot. The Bragg peak of a 62 MeV proton beam in water is shown in figure 2.2. While the Bethe Bloch equation 2.1 defines the mean energy loss per path  $\Delta x$ , the actual energy loss when passing through a material is comprised of multiple ionization and excitation processes, and therefore statistical in nature. The probability density function for a charged particle passing through an absorber  $f(\Delta E, \Delta x)$  contains a Gaussian part stemming from the multiple ionization processes with comparatively small energy transfer, and a runaway part towards high energy losses corresponding to the rare cases of high energy transfer in a single collision. Therefore, the mean value and the most probable value (the maximum of the distribution) no longer coincide. This asymmetry can be parameterized by the Vavilov parameter [6]:

$$\kappa = \frac{\xi}{W_{\max}}, \quad (2.2)$$

where  $\xi$  is the prefactor of the logarithmic term in the Bethe Bloch equation multiplied with the path length:

$$\xi = 2\pi N_A r_e^2 c^2 \rho^2 \frac{Z}{A} \frac{z^2}{\beta^2} \Delta x \quad (2.3)$$

In the case of large  $\kappa$ , the distribution is a Gaussian and therefore symmetric. The energy loss when passing through a thin layer, which corresponds to small  $\kappa$ , is described by the asymmetric Landau distribution:

$$f(x) = \frac{1}{\pi} \int_0^{\inf} e^{-slns+xs} ds. \quad (2.4)$$

For intermediate absorbers, a convolution of the two, referred to as Langauss or Langau, can be used. Figure 2.3 shows a comparison between the distributions.

### 2.1.2. Photon radiation

In particle detectors, the main contributing processes in the interaction of photons with the sensor material are the photoelectric effect, the Compton effect and pair production.

#### Photoelectric Effect

In the photoelectric effect or photoeffect, an incident photon transfers its entire energy to an atom of the traversed material, which in turn emits an electron, ionizing the atom. The photon energy  $E_\gamma$  must be higher than the binding energy of the electron  $E_b$ . The difference,  $E_b - E_\gamma$ , is passed to the emitted electron in the form of kinetic energy. The vacancy left in the inner shell can be filled by an electron from a higher shell under the emission of another photon or electron, also called Auger-electron with discrete energies. The photoelectric effect is the dominant interaction for the lower end of the photon energy spectrum.

#### Compton Effect

The Compton effect refers to the scattering of a photon with a free electron. Free in this sense meaning, that the photon's energy is much higher than the electron's binding energy. Energy and scattering angle of the photon stand in the following relation to one another:

$$E'_\gamma = \frac{E_\gamma}{1 + (E_\gamma/m_e c^2)(1 - \cos \theta_\gamma)} . \quad (2.5)$$

The difference  $E_\gamma - E'_\gamma$  is passed to the electron, and reaches a maximum at  $\theta_\gamma = 180^\circ$ .

#### Pair Production

At high energies, the photon can convert to an electron-positron pair in the Coulomb field of a charge, most commonly the atomic nucleus. For pair production, the photon energy must be higher than twice the electron resting mass:

$$E_\gamma > 2m_e c^2 = 1.022 \text{ MeV} . \quad (2.6)$$

The remaining energy,  $E_\gamma - 2m_e c^2$ , is converted to the kinetic energy of the electron positron pair.

#### Energy Deposition - Lambert Beer Law

Due to the above mentioned processes, a photon beam is attenuated inside a material according to Lambert Beer's law:

$$I(x) = I_0 \cdot e^{-\mu x} , \quad (2.7)$$

with  $I(x)$  the intensity at distance  $x$ ,  $I_0$  the initial intensity and  $\mu$  the linear attenuation coefficient.  $\mu$  is a material and photon wavelength dependent quantity.

## 2.2. Semiconductors and Detectors

In this section, semiconductors and their specific application as detectors will be briefly explained.

### 2.2.1. Semiconductors

In terms of their electrical conductivity, all solids can be divided into conductors, semiconductors and insulators. Due to the dense, periodic arrangement of the atoms in the lattice of a solid, the energy levels of the individual atoms are shifted under the influence of many neighboring atoms. The individual energy levels are energetically closely spaced on the order of meV, therefore one speaks of continuous energy bands. These bands are separated from each other by an energy gap, referred to as band gap. The highest bands, called valence and conduction bands, determine the electrical conduction properties of semiconductors. Within a single band, the energy levels are so close that transitions are easily possible and the conduction properties therefore depend on the occupation of the bands and their relative position.

In insulators, the electrons in the valence band exhibit strong binding. Due to the high band gap in insulators, it is unlikely for an electron to be thermally excited to the conduction band. Therefore, all states in the valence band are occupied and the states in the conduction band are empty and no current can flow.

In a semiconductor, the binding between the electrons is less strong, and therefore the band gap is smaller. It is more likely for an electron to pass the band gap through thermal excitation and move to the valence band, leaving behind a hole. This free electron in the conduction band and the hole in the valence band can move under the influence of an electric field, leading to current flow.

In a conductor, the conduction band is partially filled, or the valence band and conduction band overlap without a band gap. Therefore, free electrons are readily available for current conduction. A visual representation of the band structure for conductors, semiconductors and insulators can be seen in figure 2.4.

In a pure, also called intrinsic semiconductor in thermal equilibrium, the generation and recombination rates of electrons in the conduction band  $n$  and holes in the valence band  $p$ , and therefore their concentrations  $n_i$ , are equal:

$$n * p = n_i^2 = const. \quad (2.8)$$

By intentionally introducing impurities to the semiconductor, called doping, this balance can be shifted. Adding pentavalent impurities to the tetravalent semiconductor increases

the number of electrons and is called n-doping. Adding trivalent atoms increases the number of available holes and is called p-doping. Equation 2.8 also holds true for doped, or extrinsic, semiconductors. With a higher concentration of one type of charge carriers, it is easier for the the other type to find a partner for recombination.

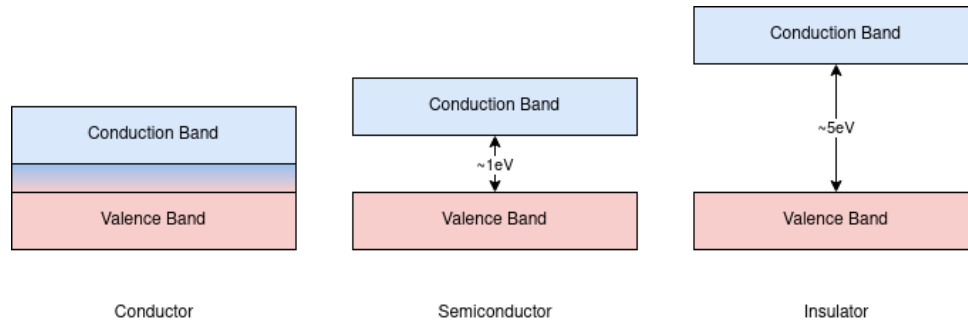


**Figure 2.4:** Schematic representation of the band structure for conductors, semiconductors and insulators. Adapted from [7]

### 2.2.2. Diode

Bringing a p-doped and n-doped semiconductor into contact with each other forms a so-called p-n-junction, or diode. At the junction, electrons from the n-doped region diffuse to the p-doped region and recombine with abundant holes. This leaves the n-doped region positively and the p-doped region negatively charged, forming an electric field opposing the diffusion, until an equilibrium is reached. This results in a built in voltage  $U_{bi}$  over the junction. The distance over which the diffusion occurs is void of free charge carriers and therefore called depletion zone. The size of the depletion zone can be influenced by applying an external voltage  $U_{ext}$  to the junction called bias voltage. Applying  $U_{ext}$  with the same polarity as  $U_{bi}$  reduces the size of the depletion zone and is called forward bias. Reversed polarity is called reverse bias and increases the size of the depletion zone.

### 2.2.3. Semiconductor Detectors

In its simplest form, a semiconductor detector is a p-n-junction operated with reverse bias. When a particle impinges on the detector and creates electron hole pairs, the resulting free charges are accelerated by the electric field present in the depletion zone. The movement of these charges, in turn, creates a measurable signal. The velocity of the charges is dependent on the local electric field:

$$\vec{v}(\vec{x}) = \mu \cdot \vec{E}(\vec{x}), \quad (2.9)$$

with the mobility  $\mu$ , which is dependent on the band structure of the semiconductor. Using a mobility model suitable for the semiconductor material in question, the mobility can be parametrized by known quantities like the doping concentration and temperature. As the number of created electron hole pairs is proportional to the deposited energy  $E_D$ ,

so is the amount of signal charge  $Q_S$ . With  $\epsilon_I$  the mean energy required for the creation of a single charge carrier pair, the total amount of collectable charge is calculated as:

$$Q_S = \frac{E_D}{\epsilon_I} \cdot e , \quad (2.10)$$

with  $e$  the charge of a single electron. With the density of silicon at  $2.33 \text{ g cm}^{-3}$  [8], the mean energy loss of a MIP in silicon can be calculated from the Bethe Bloch equation 2.1 at around  $3.87 \text{ MeV cm}^{-1}$ .  $\epsilon_I$  for silicon lies at  $3.65 \text{ eV}$  [7]. Therefore, a MIP traversing  $1 \text{ cm}$  of silicon generates around  $1.06 \times 10^6$  electron hole pairs. Compared to the intrinsic charge carrier density of silicon of  $1.01 \times 10^{10} \text{ cm}^{-3}$  [7], this value illustrates the need for depleting the sensor material of its intrinsic free charge carriers.

#### 2.2.4. Signal Formation - Shockley-Ramo Theorem

Whenever a charge is in proximity to an electrode, it influences a charge on the electrode. The amount of influenced charge is larger, the closer the charge to the electrode. If the charge itself moves, the influenced charge changes over time, which can be detected as a current. It is not necessary for a charge to reach the electrodes in order for a signal to be formed. Even if the charge is lost due to recombination or trapping, the current due to the prior movement can be registered. These circumstances are described by the Shokley-Ramo-Theorem [9] [10]. A point charge  $q$  be moving in a volume enclosed by 2 electrodes. The charge at point  $\vec{r}_q$  exerts an additional influence charge  $\Delta Q(\vec{r}_q)$  on the electrodes. The movement of the charge requires an amount of work provided by the electric field  $\vec{E}_0$  equal to:

$$dW_q = q\vec{E}_0\vec{r}_q , \quad (2.11)$$

which in turn must be provided by the voltage supply or field energy:

$$dW_q = dW_U + dW_E . \quad (2.12)$$

It can be shown that the field energy remains constant [7], and therefore the full amount of work is provided by the voltage supply as

$$dW_U = dQU . \quad (2.13)$$

With:

$$dW_q + dW_U = q\vec{E}_0\vec{r}_q + dQU \quad (2.14)$$

follows:

$$dQ = -\frac{q\vec{E}_0\vec{r}_q}{U} \quad (2.15)$$

for the influenced charge. The geometry of the electric field is solely defined by the geometry of the electrodes and is proportional to the applied voltage. Therefore, the quantity  $\vec{E}/U$  and in turn the influenced charge is independent of the applied voltage. It

is practical to define a weighting potential  $\phi_w$  and corresponding weighting field  $\vec{E}_w$  by setting  $U = 1$  in arbitrary units as

$$\phi_w = \frac{\phi_0}{U}, \quad \vec{E}_w = -\vec{\nabla}\phi_w, \quad (2.16)$$

with  $\phi_0$  defined via

$$\Delta\phi_0 = 0, \quad \vec{E}_0 = -\vec{\nabla}\phi_0. \quad (2.17)$$

The change in influenced charge can then be expressed in the following form:

$$dQ = -q\vec{E}_w d\vec{r}_q. \quad (2.18)$$

With a constant voltage between the electrodes, the movement of the charge  $v_q$  therefore creates a measurable signal current:

$$i_S = -\frac{dQ}{dt} = -q\vec{E}_w \vec{v}_q. \quad (2.19)$$

### 2.2.5. Signal Fluctuation and Fano Factor

For the creation of an electron hole pair, an incident particle has to deposit at least the energy equivalent to the band gap  $E_{\text{gap}}$  in the sensor material. The deposited energy is however statistically distributed between the creation of electron hole pairs and the excitation of phonons. Therefore, on average, an energy  $E_{e/h}$  higher than  $E_{\text{gap}}$  is necessary for the creation of a single electron hole pair. For a fixed energy deposition, the number of created pairs  $N_{e/h}$  and phonons  $N_p$  underlies Poisson statistics, and exhibit fluctuations on the order of  $\sigma_{e/h} = \sqrt{N_{e/h}}$  and  $\sigma_p = \sqrt{N_p}$ . In practice, fluctuations smaller than those expected from the Poisson statistic can be observed. This is due to an additional constraint posed by the energy conversion. When an incident particle is completely absorbed in the sensor, the total energy used for the creation of electron hole pairs  $E_i$  and for phonon excitation  $E_p$  cannot exceed the initial energy of the particles  $E_0$ :

$$E_0 = E_i \cdot N_{e/h} + E_p \cdot N_p \quad (2.20)$$

$E_0$  is however fixed for total particle absorption, and any fluctuation in the amount of energy used for phonon excitation  $E_0 \cdot \Delta N_p$  is compensated by a correspondingly smaller amount of energy used for electron hole pair creation  $E_0 \cdot (-\Delta N_{e/h})$ :

$$E_i \cdot \Delta N_{e/h} - E_p \cdot \Delta N_p = 0, \quad (2.21)$$

or averaged over many absorptions:

$$E_p \cdot \sigma_p = E_i \cdot \sigma_{e/h} \quad (2.22)$$

With this, the improved resolution can be expressed as:

$$\sigma_{e/h} = \sqrt{\frac{E_0}{E_{e/h}}} \cdot \sqrt{\frac{E_p}{E_i} \left( \frac{E_{e/h}}{E_i} - 1 \right)} = \sqrt{N_{e/h} \cdot F}, \quad (2.23)$$

with  $F$  the so called Fano factor, which takes on values between 0 and 1. Detector materials with smaller values for  $F$  have better intrinsic energy resolution.

### 2.2.6. Signal Timing

In regards to accurate signal timing, a number of aspects of the detector and readout setup play an important role, the most important of which are described here.

#### Jitter

Timing resolution is impacted by the presence of noise on the signal. This effect is called jitter and is proportional to the noise  $N$  and inversely proportional to the rise time of the signal  $t_r$ . Under the assumption of a constant slew rate, the jitter  $\sigma_{\text{jitter}}$  can be approximated as:

$$\sigma_{\text{jitter}} = \frac{N}{dS/dt} \approx \frac{t_r}{S/N} . \quad (2.24)$$

$\sigma_{\text{jitter}}$  is therefore inversely proportional to the signal to noise ratio. A visual explanation of jitter and the ensuing uncertainty is shown in figure 2.5.

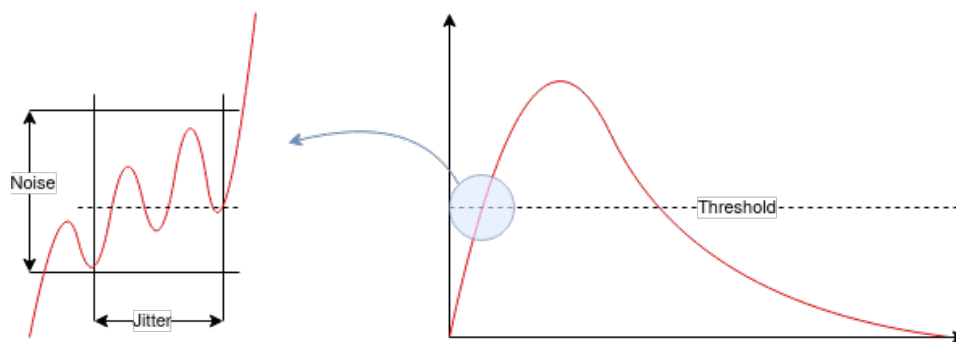


Figure 2.5: On the uncertainty arising from jitter. Adapted from [11].

#### Time walk

Due to the different total amount of generated charge carriers, signals with different peak values are generated. Signals with the same shape but different amplitude cross the same fixed threshold at different times. This phenomenon is called time walk and is visualized in figure 2.6. Under the assumption that the signal shape does not distort for different amplitudes, time walk can be combated by using a constant fraction discriminator (CFD) instead of a fixed threshold. With this method, the arrival time is instead set at the crossing of a fixed fraction of the signal amplitude.

#### Landau Noise

Due to the different spatial distribution of the charge carriers, irregularly shaped signals can arise for the same number of generated charge carriers. As the shape of the signal influences the time, at which a threshold is reached, this effect also negatively impacts the timing resolution.

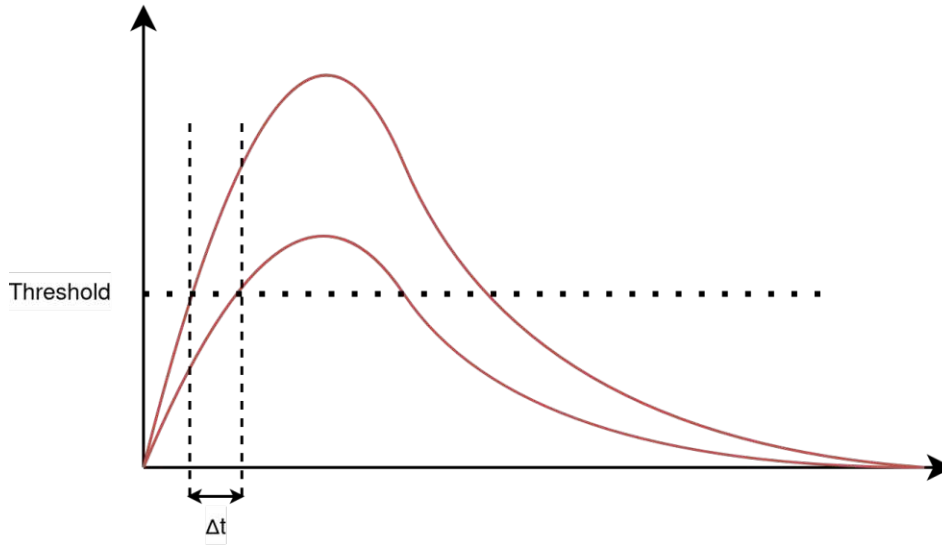


Figure 2.6: Time walk stemming from signals with different peak values. Adapted from [11].

### Signal Distortion

As the signal depends on the weighting field and charge carrier velocity as described in section 2.2.4, any irregularities in those quantities influence time resolution negatively. If the charge carrier velocity is not saturated, or the weighting field is not uniform, the signal shape depends on the location of the ionization event. For a fully depleted detector with planar geometry, this form of distortion can be neglected. It is more prevalent for the more complicated geometries found for example in segmented readout electrodes like strip or pixel detectors.

Additionally, a factor stemming from the finite size of the digitized signal's bin width  $\Delta t$  has to be taken into consideration. This uncertainty is equal to:

$$\sigma_{\text{TDC}} = \frac{\Delta t}{\sqrt{12}} \quad (2.25)$$

The overall time resolution  $\sigma_t$  can then be calculated as:

$$\sigma_t^2 = \sigma_{\text{jitter}}^2 + \sigma_{\text{ionization}}^2 + \sigma_{\text{distortion}}^2 + \sigma_{\text{TDC}}^2 \quad (2.26)$$

By using an oscilloscope with an adequate sampling rate this effect can be minimized.

### 2.3. Silicon Carbide

Silicon carbide (SiC) occurs in a number of different polytypes with different stacking sequences. SiC, and in particular its 4H-SiC polytype, exhibits a number of physical properties, that make it an interesting candidate as an alternative to silicon [12]. Its high band gap, around twice that of silicon, results in much lower leakage currents. In combination with the high thermal conductivity, temperature control of the sensor is simplified. The high displacement energy reduces the frequency of defect formation, making SiC potentially more radiation hard. Furthermore, the higher saturation velocity of charge carriers in SiC increases the intrinsic time resolution of the sensor. With the high breakdown field of SiC, the saturation velocities can easily be reached. Table 2.2 lists the mentioned physical properties for Si and SiC.

Property	Silicon	4H-SiC	Unit	
Bandgap	1.12	3.26	eV	
Energy to create an e-h-pair	3.6	7.78	eV	
MIP ionisation density	80	57	$\mu\text{m}^{-1}$	
Electron saturation velocity	$1.0 \times 10^7$	$2.2 \times 10^7$	$\text{cm s}^{-1}$	
Hole saturation velocity	$0.9 \times 10^7$	$1.3 \times 10^7$	$\text{cm s}^{-1}$	
Breakdown field for a doping density of $10^{16} \text{ cm}^{-3}$	0.3		$\text{MV cm}^{-1}$	
		parallel to c-axis	2.8	$\text{MV cm}^{-1}$
		perpendicular to c-axis	2.2	$\text{MV cm}^{-1}$
Thermal conductivity	1.3 - 1.5	3.3 - 4.9	$\text{W cm}^{-1} \text{ K}^{-1}$	
Atomic displacement energy	13 - 20		eV	
		Si	66	eV
		C	24	eV

**Table 2.2:** Comparison between Si and SiC properties [12–15]. c-axis refers to the stacking orientation.

## 3. Materials and Methods

### 3.1. AllPix<sup>2</sup>

AllPix<sup>2</sup> [16] is a semiconductor detector simulation framework written in C++. It builds upon packages well known in the high energy physics field such as Geant4 [17] for the interaction of radiation with the sensor and ROOT [18] for the data analysis and storage. The framework is comprised of a central core that separates the common infrastructure from the individual modules responsible for the physical simulation steps. This structure is shown in figure 3.1. A simple simulation chain using a single detector is visualized in figure 3.2. The simulation chain begins with the passage of ionizing radiation through the sensor material and ends with the digitization by the readout electronics. Each simulation step is performed by a so-called module, which are configured in a .ini-like format. In general, the individual modules take output-objects of other modules as input objects and then produce new output-objects for further processing by the next module. The interaction between the modules is performed by a messaging system of the AllPix<sup>2</sup> framework. The framework also records the full object history, allowing for a complete reconstruction of the simulation.

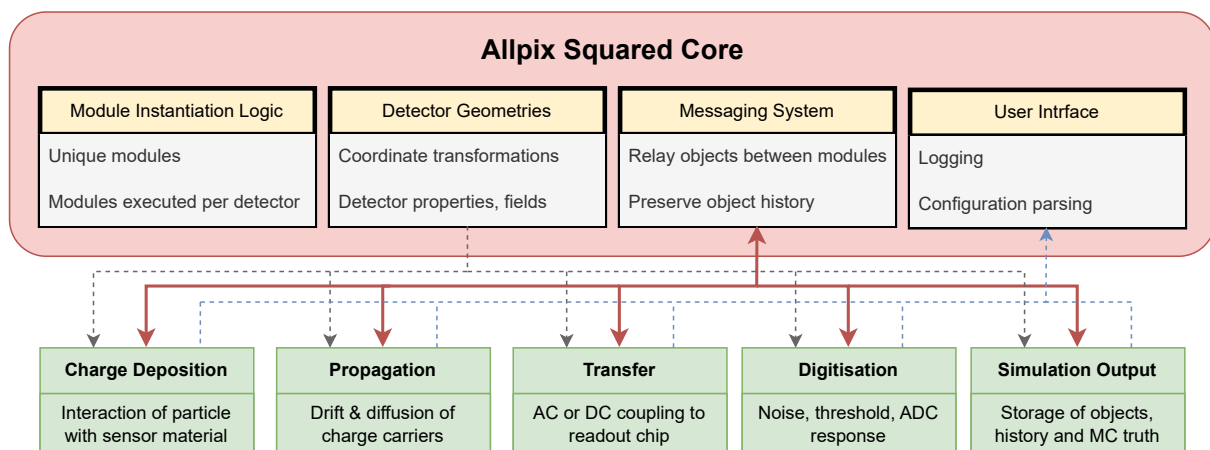


**Figure 3.1:** Structure of the AllPix<sup>2</sup> framework with the framework core and individual modules. The passing of detector configuration information is indicated by the grey dashed arrows. The red arrows represent the interaction of the modules via the messaging system. Logging information is passed back along the blue dashed arrows. Adapted from [19].

#### 3.1.1. Deposition

The simulation chain begins by creating charges in the active sensor material according to the incident radiation. This is performed by a Deposition module. The two modules used in the scope of this work are the `DepositionPointCharge` and the `DepositionGeant4`

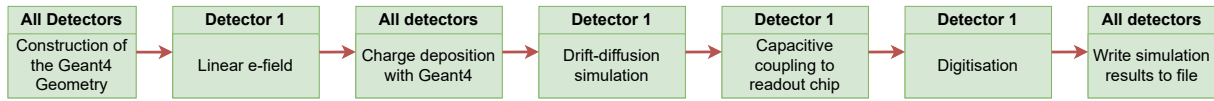


**Figure 3.2:** Setup of an Allpix2 simulation using a single detector, where every block represents a single module instantiation. After the geometry construction and field setup, charge carriers are deposited, propagated and collected at the implants. Finally, the resulting signal is digitised and the results are stored. Adapted from [19].

modules. The deposition modules produce `DepositedCharge` objects for further processing.

### DepositionPointCharge

The `DepositionPointCharge` module is used to create a defined number of electron-hole-pairs, either at a specific point, or along a straight line. In this work, it was used to simulate the energy deposition exhibited by the UV-Laser.

### DepositionGeant4

To accurately simulate the more complex interaction of primary particles with the detector material, a wrapper module for the Geant4 simulation toolkit is available in the form of the `DepositionGeant4` module. With this module, primary sources of different shapes and particle types can be defined. For each of the primary particles, the energy loss within the active sensor material at each simulation step is converted into a number of charge carriers, depending on the mean pair creation energy and the Fano factor of the material in question.

#### 3.1.2. Propagation

After the creation of electrons and holes in the sensor, these charges are propagated through the sensor. This is performed by a propagation module. The propagation module takes the generated `DepositedCharge` objects, propagates the corresponding charges through the sensor and generates `PropagatedCharge` objects for further processing. For this thesis, the `GenericPropagation` and `TransientPropagation` were used. These modules provide a visualization mechanism of the propagation called line graphs. An example line graph is shown in figure 3.4.

### ElectricFieldReader

For the propagation of the charge carriers, an electric field must be present in the sensor. This electric field is provided by the `ElectricFieldReader` module. The field can either be generated according to a custom or predefined formula, or loaded from the mesh of a corresponding TCAD simulation.

### WeightingPotentialReader

If precise simulation of the transient output pulse is desired, the induced charge on the pixels must be calculated according to the Shokley-Ramo-Theorem. For this, a weighting potential is required as described in section 2.2.4. This is provided by the `WeightingPotentialReader`. The weighting potential can again be provided in the form of a mesh from a TCAD simulation. Alternatively, the weighting potential of a pixel in a plane condenser can be calculated according to the procedure in [20].

### GenericPropagation

The `GenericPropagation` module simulates the movement of the charge carriers through the active sensor material as a combination of drift and diffusion. For this, the mobility at each simulation point is calculated using the defined mobility model. The drift propagation is estimated using a fourth-order Runge-Kutta-Fehlberg method. After the drift step, the diffusion is drawn from a Gaussian distribution with  $\sigma = \sqrt{\frac{2k_B T}{e} \mu t}$ , where  $t$  is the size of the time-step,  $\mu$  the mobility and  $T$  the temperature. This module does not provide any pulse information.

### TransientPropagation

In the `TransientPropagation` module, the charge propagation works identically to the `GenericPropagation` module. Additionally, after each time-step, the induced charge on the electrodes is calculated according to the Shockley-Ramo-Theorem as explained in section 2.2.4. This is done by taking the difference between the weighting potential at the position before and after the time-step, and multiplying by the charge.

$$Q_{\text{ind}} = q (\phi(x_{\text{curr}}) - \phi(x_{\text{prev}})) \quad (3.1)$$

This results in an individual pulse for each charge carrier, which need to be combined by a transfer module.

### Mobility Models

For the simulations, the extended Jacoboni Canali model was expanded with a parameter set suitable for SiC. This model combines the doping concentration dependent low field mobility of the Masetti model [21] with the high field mobility of the Jacoboni Canali model [22] according to:

$$\mu(E, N) = \frac{\mu_m(N)}{(1 + (\mu_m(N) \cdot E/v_m)^\gamma)^{1/\gamma}}, \quad (3.2)$$

with  $\mu_m(N)$  the Masetti mobility as:

$$\begin{aligned}\mu_{m,e}(N) &= \mu_{0,e} + \frac{\mu_{\max,e} - \mu_{0,e}}{1 + (N/C_{r,e})^{\alpha_e}} - \frac{\mu_{1,e}}{1 + (C_{s,e}/N)^{\beta_e}} \\ \mu_{m,h}(N) &= \mu_{0,h} \cdot e^{-P_c/N} + \frac{\mu_{\max,h} - \mu_{0,h}}{1 + (N/C_{r,h})^{\alpha_h}} - \frac{\mu_{1,h}}{1 + (C_{s,h}/N)^{\beta_h}},\end{aligned}\quad (3.3)$$

for electrons and holes respectively. The adapted parameters are listed in table 3.3. According to equation 3.3, the low field mobility decreases for increasing doping concentration and exhibits a 'min-max' behaviour dictated by the first two terms. The dominant contributor to this mobility decrease is an increase in scattering of the charge carriers at ionized impurities. The third term, which in the case of the chosen parameters is always 0, describes the additional decrease of the low field mobility for extremely high doping concentrations. Equation 3.2 captures the breakdown of the linear relationship between electric field strength and resulting drift velocity for high fields. Visualizations of the low field mobility as well as the high field mobility and resulting charge carrier velocity using the custom SiC parameter set can be seen in figure 3.3.

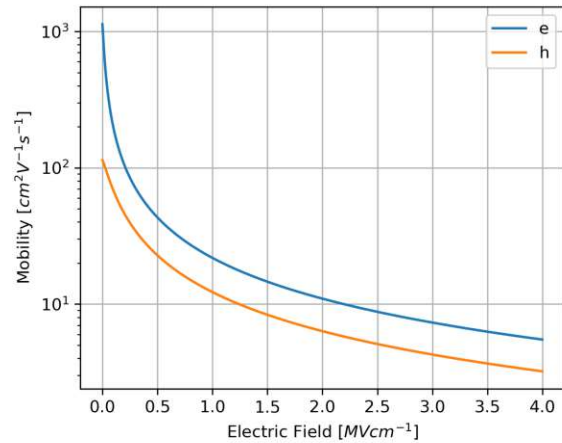
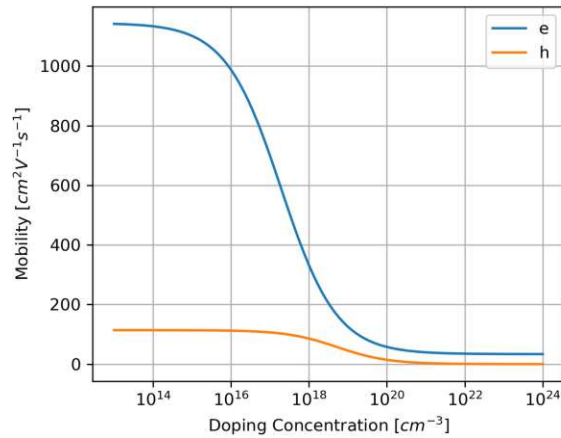
Parameter	Electron	Hole	Unit
$v_m$	$1.8851 \times 10^7 / 2.2 \times 10^7$	$1.3 \times 10^7$	$\text{cm s}^{-1}$
$\gamma$	1.2	1.2	
$\mu_{\max}$	950 / 1144.5783	114.10 / 99.2174	$\text{cm}^2 \text{V}^{-1} \text{s}^{-1}$
$\mu_0$	27.87 / 33.5783	0	$\text{cm}^2 \text{V}^{-1} \text{s}^{-1}$
$\mu_1$	0	0	$\text{cm}^2 \text{V}^{-1} \text{s}^{-1}$
$\alpha$	0.61	0.66	
$\beta$	0	0	
$C_r$	$1.94 \times 10^{17}$	$5.38 \times 10^{18}$	$\text{cm}^{-3}$
$C_s$	0	0	$\text{cm}^{-3}$
$P_c$		0	$\text{cm}^{-3}$

**Table 3.3:** Used parameters for the Masetti Canali model. Since the mobility is anisotropic, two values are given for the relevant parameters where available. The first value represents perpendicular, the second movement parallel to the c-axis. Temperature dependence was neglected and the parameters are therefore only valid at 300 K. The values were taken from [12, 23–25]. The anisotropy was calculated using the factor found in [26].

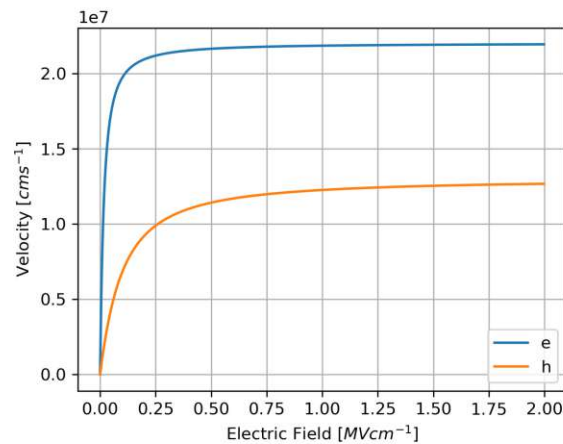
### Weighting Field Calculation

As explained in section 2.2.4, a weighting field is necessary for characterization of the transient pulses. This weighting field  $\phi_w(\vec{r})$  can be calculated from the electrostatic potentials  $\phi_1(\vec{r})$ ,  $\phi_2(\vec{r})$  from accompanying TCAD simulations at two slightly different bias voltages  $V_{b,1}$  and  $V_{b,2}$  as:

$$\phi_w(\vec{r}) = \frac{\phi_1(\vec{r}) - \phi_2(\vec{r})}{V_{b,1} - V_{b,2}}. \quad (3.4)$$



(a) Doping concentration dependent low field mobility of electrons and holes (b) High field mobility at a doping concentration of  $1.5 \times 10^{14} \text{ cm}^{-3}$ .



(c) Resulting charge carrier velocities at a doping concentration of  $1.5 \times 10^{14} \text{ cm}^{-3}$ .

**Figure 3.3:** Visualization of the low field mobility versus doping concentration, and the high field mobility and resulting velocities at a fixed doping concentration for electrons and holes.

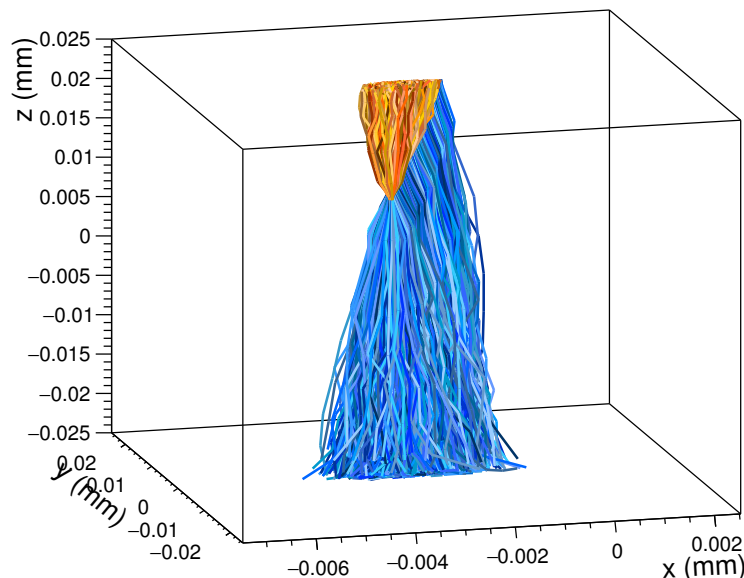


**Figure 3.4:** Linegraph of the charge carriers created by an alpha particle hitting an idealized sensor (linear E-field) at an angle. The electrons are colored in blue, the holes in orange.

### 3.1.3. PulseTransfer

The individual pulses created by the propagated charge carriers need to be prepared for digitization by the front end electronics. This is performed by the `PulseTransfer` module. It takes the `PropagatedCharge` objects of the Propagation module and creates `PixelCharge` objects ready for digitization. If the `PropagatedCharge` objects provided by the Propagation module provide no pulse information themselves, e.g. if the `GenericPropagation` module is used, a pseudo-pulse is generated from their arrival times. Using the parameter `max_depth_distance`, the depth a particle has to reach during propagation to be taken into account, can be set.

### 3.1.4. CSADigitizer

Once the charges have been propagated, the induced pulses at the electrodes need to be digitized. In the scope of this work, this was performed using the `CSADigitizer` module with a custom transfer function.

### 3.1.5. ROOTObjectWriter

For data analysis, the contents of the messages exchanged by the individual modules are required. Using the `ROOTObjectWriter` module, these messages, or a specified subset thereof, can be saved to disk. The message objects relevant in this work are:

- `DepositedCharge` ... Information about the generated charge carriers
- `PropagatedCharge` ... Information about the charge carriers after propagation
- `PixelCharge` ... Current at the pixel
- `PixelPulse` ... Digitized signal at the pixel

A summarization of the Python code used to extract this information from the output ROOT file in a manageable manner is shown in A.3.

## 3.2. Pulse Analyzer

For analysis of the digitized output signal, a Python based software developed at HEPHY was used [27]. After setting a number of configuration parameters such as a threshold or CFD, it is capable of extracting a set of quantities for each pulse found. Among those quantities are:

- Start time [ns]
- Interpolated start time [ns]
- Signal maximum [mV]
- Noise RMS [mV]
- Peak area [V s]

The software also includes a GUI, which can be very useful for quickly analyzing or debugging the result data. A screenshot of an analyzed example waveform can be seen in figure 3.5. A custom readout class was implemented for the software to work with the data produced by AllPix<sup>2</sup> using the PyROOT python package supplied by ROOT.

### 3.2.1. Time Resolution Measurement

The 'start time' parameter provided by the analysis software indicates the time point of the first sample above the threshold. For the 'interpolated start time', a linear function is fitted to the last sample under and the first sample over the threshold. This is used to combat the impact of TDC on the time resolution explained in section 2.2.6. The standard

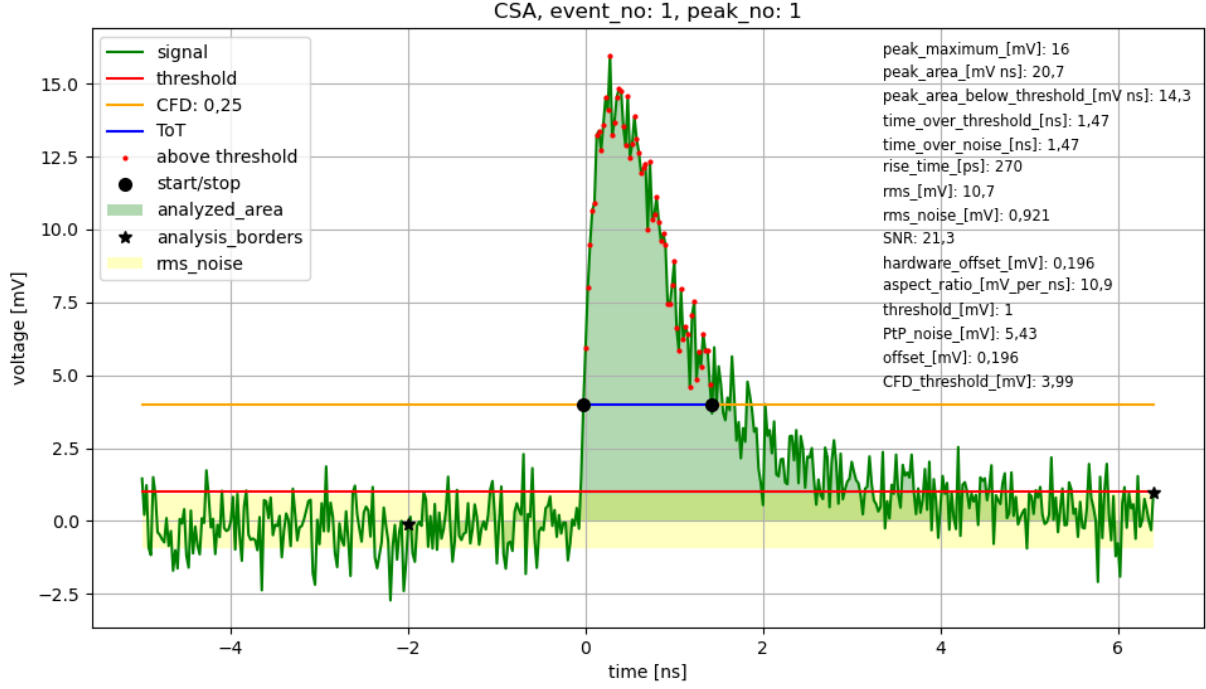


Figure 3.5: Screenshot of an analyzed waveform in the GUI of the Pulse Analyzer software.

deviations of the 'start time' and 'interpolated start time' parameters are interpreted as the observed time resolution  $\sigma_t$ :

$$\sigma_t = \sqrt{\frac{\sum (t_i - \bar{t})^2}{n - 1}}, \quad (3.5)$$

where  $t_i$  is the timepoint of the  $i$ 'th acquisition,  $\bar{t}$  the mean timepoint and  $n$  the number of acquisitions.

### 3.2.2. Charge Collection Efficiency

Charge collection efficiency (CCE) is defined as the fraction of collected charge  $Q_{\text{col}}$  and the total charge deposited during an ionization event  $Q_{\text{dep}}$

$$CCE = \frac{Q_{\text{col}}}{Q_{\text{dep}}}. \quad (3.6)$$

The CCE gives information about the size of the depleted region in the sensor, as only the charges generated within the depletion zone experience an electric field and are therefore accelerated. In a fully depleted sensor, the CCE approaches 100%. As the total amount of deposited charge is generally unknown, the CCE can also be defined in relation to the maximum observed collected charge, which is proportional to the peak area of the signal. With AllPix<sup>2</sup> however, the generated charges are available in the form of the DepositedCharge messages.

### 3.3. Detector Prototype

The experiments were performed on a planar SiC pad detector produced at IMB-CNM-CSIC [28] in Barcelona. It features a 50  $\mu\text{m}$  thick,  $3 \times 3 \text{ mm}$  active area, epitaxially grown on a 4H SiC substrate. The total dimensions of the sensor are  $4400 \times 4400 \times 400 \mu\text{m}$ . The p-on-n type sensor has an n-doped active area with strongly p-doped implants on top. The 1.02  $\mu\text{m}$  thick metallization layer consists of aluminum, nickel, and titanium. The additional passivation layer consists of 150 nm of  $\text{SiO}_2$  and  $\text{Si}_3\text{N}_4$ . A schematic cross section of this design can be seen in figure 3.6. This detector was modeled in AllPix<sup>2</sup> with the `detector.conf` file shown in configuration 1. The materials `silicon_dioxide` and `silicon_nitride` needed to be implemented in the `MaterialManager` of the AllPix<sup>2</sup> framework. The densities used are  $\rho_{\text{SiO}_2} = 3.17 \text{ g cm}^{-3}$  and  $\rho_{\text{Si}_3\text{N}_4} = 2.65 \text{ g cm}^{-3}$  [29].

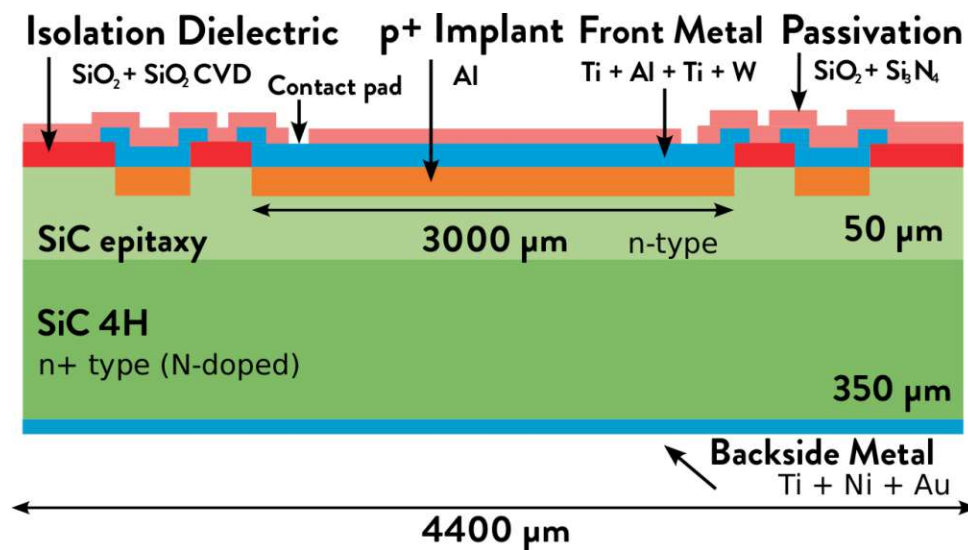


Figure 3.6: Schematic cross section of the detector in use in the experiments [30].

```
1 # Detector configuration
2 type = "monolithic"
3 geometry = "pixel"
4 number_of_pixels = 1 1
5 pixel_size = 3mm 3mm
6 implant_size = 3mm 3mm
7 sensor_thickness = 50um
8 sensor_excess = 0um
9 sensor_material = "silicon_carbide"
10
11 [support]
12 size = 3mm 3mm
13 thickness = ###.nm
14 location = chip
15 material = "titanium"
16
17 [support]
18 size = 3mm 3mm
19 thickness = ###.nm
20 location = chip
21 material = "aluminum"
22
23 [support]
24 size = 3mm 3mm
25 thickness = ###.nm
26 location = chip
27 material = "nickel"
28
29 [support]
30 size = 3mm 3mm
31 thickness = ###.nm
32 location = chip
33 material = "SILICON_DIOXIDE"
34
35 [support]
36 size = 3mm 3mm
37 thickness = ###.nm
38 location = chip
39 material = "silicon_nitride"
```

**Configuration 1:** Configuration of the detector in AllPix<sup>2</sup>. The exact dimensions of the metallization layer are omitted due to NDA constraints.

### 3.4. Readout Electronics

The readout of the sensor was carried out by two different amplifiers. The UCSCSingleChannel and the Cividec Cx-L.

#### 3.4.1. UCSCSingleChannel Amplifier

The UCSCSingleChannel is an inverting transimpedance amplifier (TIA) based on an AC-coupled silicon-germanium bipolar transistor in a common emitter configuration. Amplification is performed with a  $\sim 2$  GHz bandwidth and a 29 dB gain at 1.9 GHz [31, 32]. A bode plot of the measured transfer function of this amplifier and a fit of the function:

$$H(f) = \frac{A}{\sqrt{f^2 t_1^2 + 1} \cdot \sqrt{f^2 t_2^2 + 1}}, \quad (3.7)$$

with the determined fit parameters:

$$\begin{aligned} A &= 389 \text{ V A}^{-1} \\ t_1 &= t_2 = 2.594 \text{ ns} \end{aligned} \quad (3.8)$$

can be seen in figure 3.7. Readout of the UCSCSingleChannel was performed by a Rhode & Schwarz RTP164 oscilloscope with  $40 \text{ GS s}^{-1}$  and an analog bandwidth of 16 GHz.

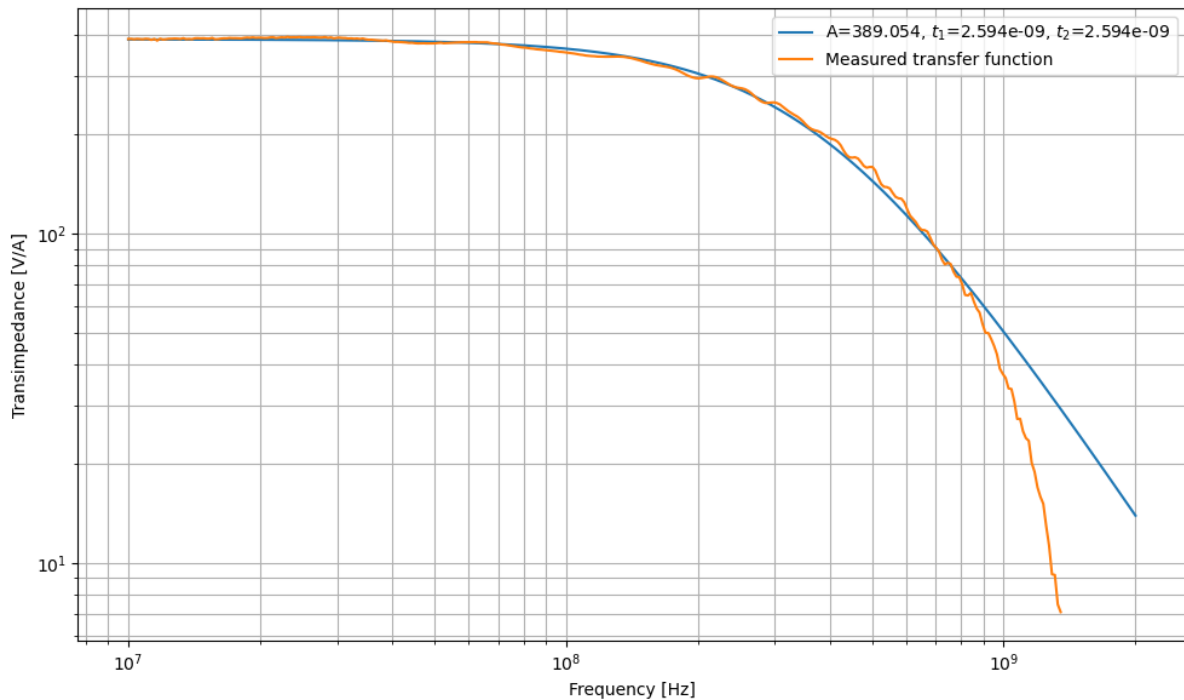


**Figure 3.7:** Measured bode plot of the UCSCSingleChannel (orange) and best fit of function 3.7 to the measured data (blue).

### 3.4.2. Cividex Cx-L

The Cividex Cx-L is a charge sensitive amplifier (CSA) with a Gaussian pulse shape with a FWHM of 180 ns and a rise time of 80 ns [33]. The amplifier readout was performed by a Rhode & Schwarz RTO6 oscilloscope with  $10 \text{ GS s}^{-1}$  and an analog bandwidth of 50 MHz. This amplifier was not directly modelled in the simulations. As the amplifier is charge sensitive, the signal height is directly proportional to the amount generated charge carriers and can therefore be equated to the information stored in the `DepositedCharge` objects of AllPix<sup>2</sup>.

## 3.5. TCAD Fields

As can be seen in the results of this work, accurate knowledge of the electric field, doping concentration and weighting field of the simulated sensor is required. This usually comes in the form of TCAD simulations. The used fields in this work were taken from accompanying simulations in the Synopsys [34] suite. The simulations were performed and the results provided by. Two 2-dimensional sections of the active sensor area were simulated. The first is a  $50 \mu\text{m}$  wide strip at the center of the pad region. Simulations were run at 1 V increments of the applied bias voltage from 0 V to 2001 V. The second area is a  $256 \mu\text{m}$  wide region at the edge of the pad region, including the guard ring structure. Simulations were run at 50 V steps, including a 1 V increment for each step from 0 V to 2000 V (0, 1, 50, 51, ... 2000, 2001).

### 3.5.1. Workflow

The step-by-step workflow to extract the relevant information from the output files of the Synopsys TCAD simulation is described here. Some examples of the resulting TCAD fields are shown in figures 3.8 to 3.11.

- 1. Convert .tdr file to the DF-ISE format** Using the `tdx` shell program of the Sentaurus Data Explorer, the `.tdx` files can be converted to a number of different formats. Among those formats is the DF-ISE format, which is known to AllPix<sup>2</sup>. The DF-ISE format consists of two files, a `.grd` and a `.dat` file, which hold the grid points and the values of the physical quantities at those points respectively. To convert to DF-ISE, `tdx --tdr2dfise <file.tdr>` was executed for every file.

- 2. Extract fields from DF-ISE** The `mesh_converter` tool provided by AllPix<sup>2</sup> is now able to extract the individual fields from the DF-ISE files, and save them in either the binary `.apf` or the text based `.init` format. The binary format provides increased performance, precision and storage efficiency, the text based format provides the benefit of being human readable, which can be helpful in further processing of the data. Since the input and output grids generally do not match, interpolation is also supported by the `mesh_converter` tool. A configuration file needs to be provided for

each physical quantity to be extracted. The quantities in question are the doping concentration, electric field and electrostatic potential. The latter is used in the last step to calculate the weighting potential and therefore needs to be saved in the `.init` format. The doping concentration and electric field can be saved in the `.apf` format. The corresponding configurations in the case of the edge region can be seen in the configurations 2, 3 and 4. This results in a regular mesh grid with a step size of  $1\mu\text{m}$  in the  $y$  direction and a step size of  $10\text{nm}$  in the  $z$  direction. Note that the TCAD fields are  $1\mu\text{m}$  larger in the  $z$  direction as compared to the detector definition in configuration 1. This is the additionally simulated buffer layer at the bottom of the active area, that was subsequently cut off before applying the TCAD field to the sensor in AllPix<sup>2</sup>.

```

1 region = "sensor"
2 observable = "DopingConcentration"
3 observable_units = "/cm/cm/cm"
4 xyz = x z -y
5 radius_step = 0.1um
6 initial_radius = 0.1um
7 divisions = 256,5100

```

**Configuration 2:** Configuration for extraction of the doping concentration

```

1 region = "sensor"
2 observable = "ElectricField"
3 observable_units = "V/cm"
4 xyz = x z -y
5 radius_step = 0.1um
6 initial_radius = 1um
7 divisions = 256,5100

```

**Configuration 3:** Configuration for extraction of the electric field

```

1 region = "sensor"
2 observable = "ElectrostaticPotential"
3 observable_units = "V"
4 xyz = x z -y
5 radius_step = 0.1um
6 initial_radius = 1um
7 divisions = 256,5100
8 model = "INIT"

```

**Configuration 4:** Configuration for extraction of the electrostatic potential

**3. Calculate Weighting Potential** Using the electrostatic potential extracted in step 2, the weighting potential can be calculated according to 3.1.2, using the simulations at 1 V increment in applied bias voltage. This was performed in Python using the text-based `.init` fields extracted in the previous step. The Python code is shown in A.2.

Figures 3.8, 3.9 and 3.10 showcase the extracted fields from the sensor's pad edge region. Spikes in the magnitude of the electric field at the edges of the implants can be observed. A comparison of the pad centre's electric field  $z$  component at different bias voltages to the linear electric field implemented in AllPix<sup>2</sup> is given in figure 3.11. For the most part, the TCAD field also behaves in a linear fashion. Only near the junction with the substrate, a steep decline in the field strength can be observed, as the doping concentration quickly rises.

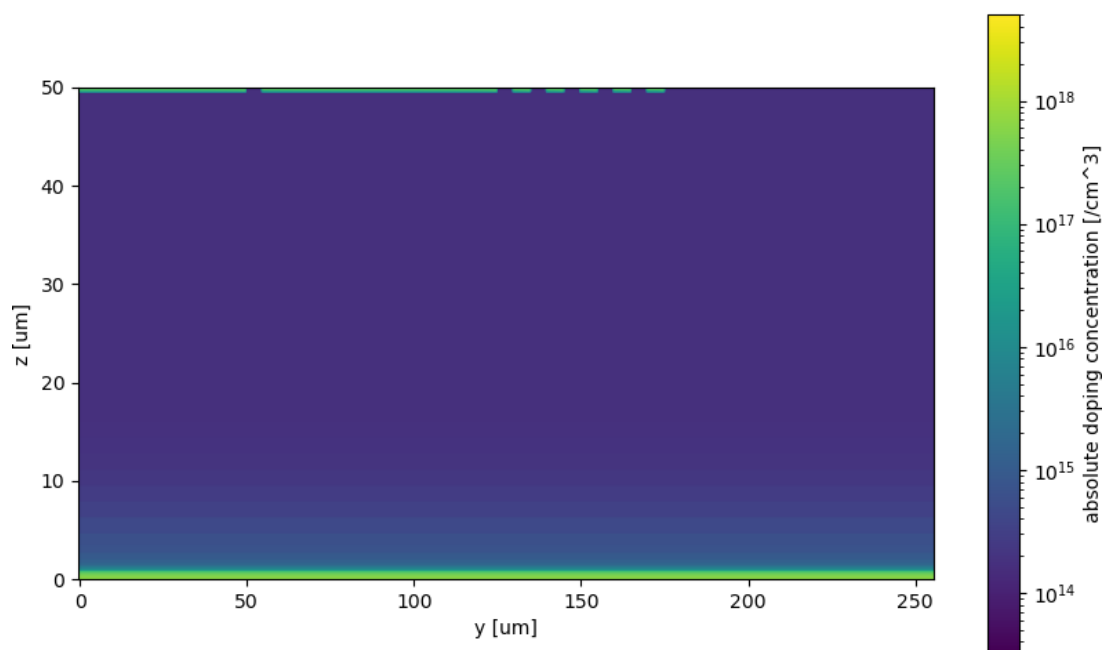


**Figure 3.8:** (Absolute) doping concentration of the TCAD simulated area at the edge of the pad region.

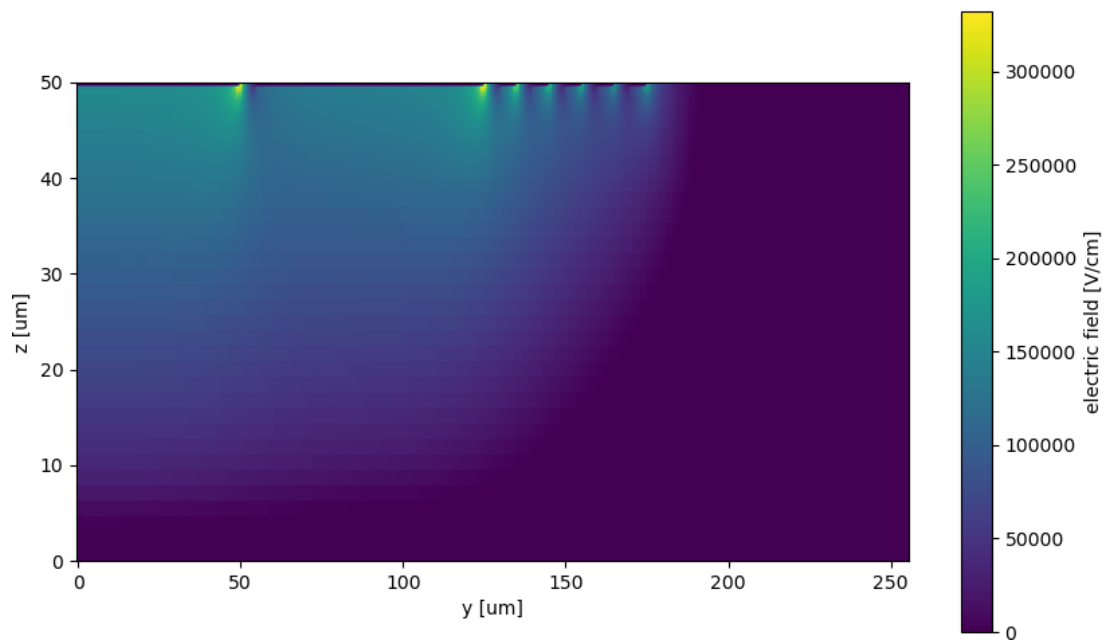


**Figure 3.9:** Electric field of the TCAD simulation at the edge of the pad region with a bias voltage of 400 V.

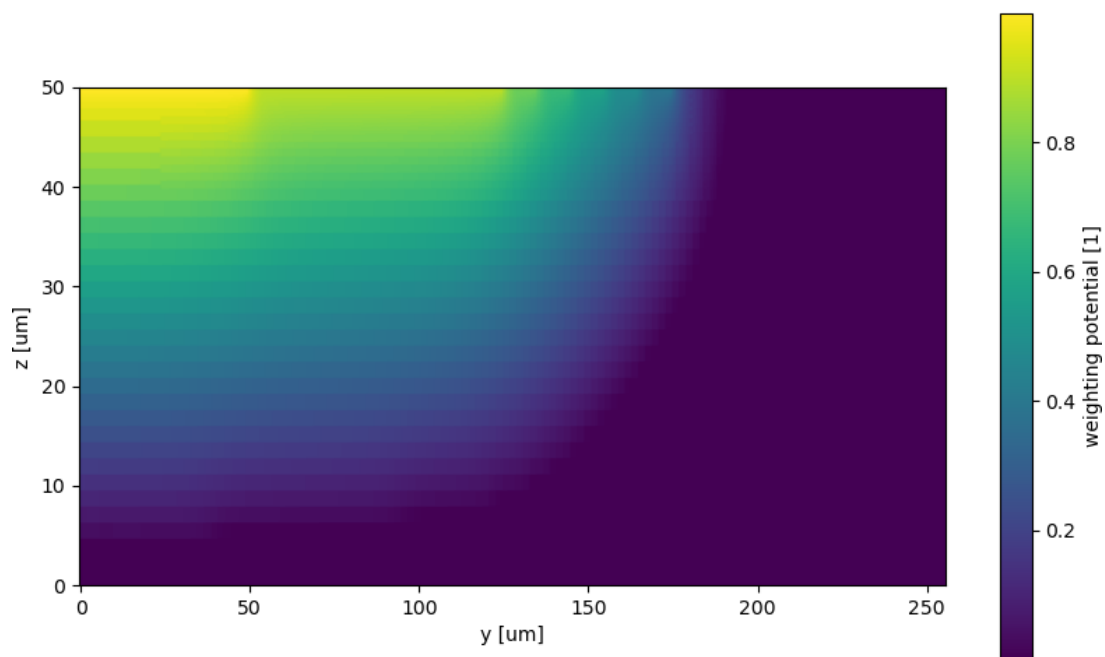


**Figure 3.10:** Weighting potential calculated from the electrostatic potential of the TCAD simulation at the edge of the pad region with a bias voltage of 400 V.

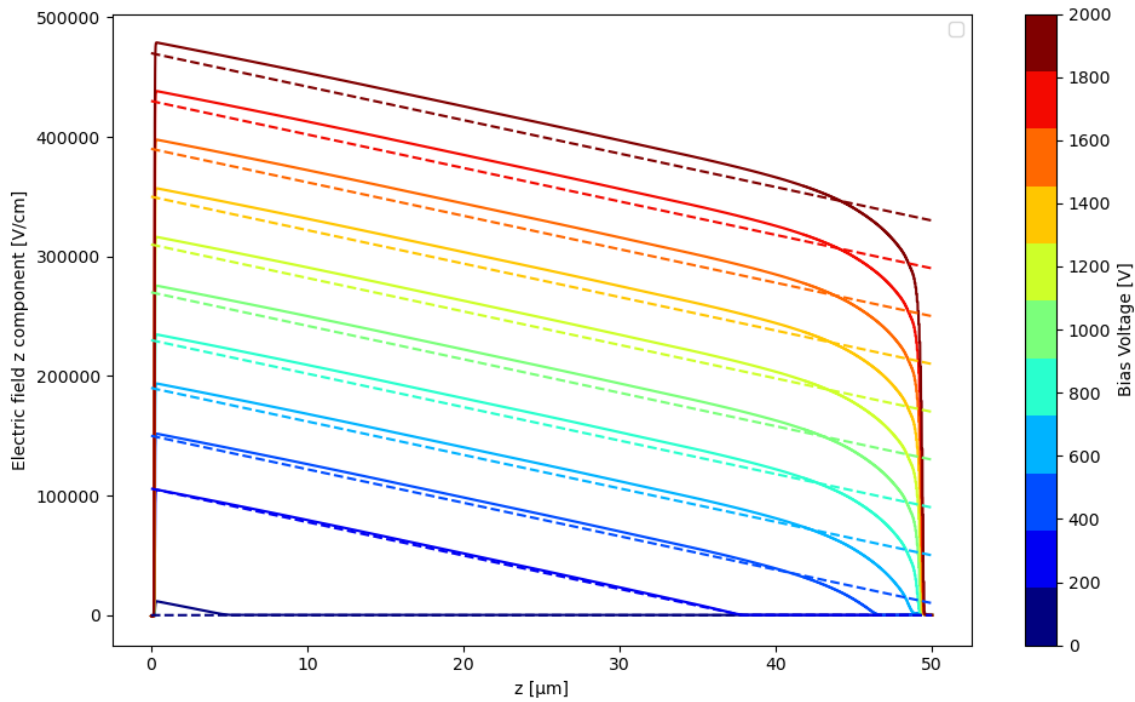


**Figure 3.11:** Comparison between the analytical linear field for a full depletion voltage of 350 V available in AllPix<sup>2</sup> and the simulated TCAD field at different applied bias voltages.

## 3.6. Simulation Workflow

### 3.6.1. HTCCondor

To speed up the process of running the simulations, a cluster of servers and personal computers running the HTCCondor software suite [35], an open-source high-throughput computing software framework developed at the university of Wisconsin-Madison, was used. In HTCCondor, the total workload can be divided into atomic units of work called jobs. Each job is then assigned to any of the available nodes in the HTCCondor network.

### 3.6.2. Docker

Docker is a platform for packaging an application, including all of its dependencies and the underlying infrastructure into so called containers for easy distribution. The individual HTCCondor jobs were run in Docker containers to ensure a consistent environment across all simulations. A private fork of the main AllPix<sup>2</sup> repository in version 2.0 was created. This repository contains the changes made to the AllPix<sup>2</sup> source code, such as the Jacoboni-Canali mobility parameters for SiC. Using the Dockerfile already provided by AllPix<sup>2</sup>, an image was built and pushed to the docker registry at HEPHY with the following commands:

```

1 docker build -t registry.gitlab.com/dd-hephy/hibpm/allpix-squared-fork:
  dev --file etc/docker/Dockerfile .
2 docker push registry.gitlab.com/dd-hephy/hibpm/allpix-squared-fork:dev

```

This image can then be used in the HTCondor submit file by including the following lines in the configuration:

```

1 universe = docker
2 docker_image = registry.gitlab.com/dd-hephy/hibpm/allpix-squared-fork:
  dev

```

### 3.6.3. Simluation Scans

The evaluation of the quantities looked at in the scope of this work required scanning over certain parameters in the AllPix<sup>2</sup> configuration, such as the applied TCAD fields (in essence the applied bias voltage), or the `number_of_charges` parameter of the `DepositionPointCharge` module. This was realized within the HTCondor submit files, by issuing a job for each data point. The individual jobs were run on a single core, as the number of data points already exceeded the number of available cores in the HTCondor network and therefore no additional performance would be gained from parallel computation of the individual events for each data point.

### CCE Evaluations

To determine the CCE versus applied bias voltage, the simulations were repeated using different applied TCAD fields in the case of the Transient-TCAD and Generic-TCAD setups, and different values for the `bias_voltage` parameter of the `ElectricFieldReader` module for the Transient-Linear and Generic-Linear simulations. Per data point, 10 events were simulated for the UV-Laser simulations, 10000 for the proton and 3333 events per nuclide for the alpha simulations.

### Time Resolution

For the determination of the time resolution at different signal intensities, single noise free events using different values for the `number_of_charges` parameter of the `DepositionPointCharge` module were resampled with gaussian noise to create 10000 pseudo events per data point. This yields a sufficiently large sample size to calculate the time resolution  $\sigma_t$  according to equation 3.5. This simplification was deemed acceptable, as the charge deposition using the `DepositionPointCharge` module is deterministic, and any effects stemming from the diffusion of the individual charge carriers is expected to average out across the high number of charges (on the order of  $10^5$  charges per event).

### 3.7. Experimental Setups

All simulations were run with the intention of reproducing the results of experiments with a SiC detector at HEPHY. The results of the experiments in question were provided by Andreas Gsponer. The setups of the experiments and corresponding AllPix<sup>2</sup> simulations using the three investigated radiation types (UV-laser, proton and alpha), are described in this section.

#### 3.7.1. UV-Laser Experiments

##### Experiment Setup

The SiC sensor was irradiated with the light of a Pilas DX PIL037-FC laser diode with a nominal wavelength of  $(375 \pm 10)$  nm and pulse width of  $<70$  ps [36]. This wavelength corresponds to a photon energy of  $E_\gamma = 3.306$  eV, which is just above the bandgap of SiC. The continuous power output was measured at 6.2 nW at a repetition rate of 500 Hz. The absorption coefficient for 370 nm wavelength light lies at  $42.25 \text{ cm}^{-1}$  [37]. The quantum efficiency for a 50  $\mu\text{m}$  thick SiC sensor is therefore 19.04%. This behaviour is visualized in figure 3.12. The total amount of energy deposited in the sensor material per event is therefore 14.7 MeV. This corresponds to  $4.027 \times 10^6$  electron hole pairs generated. Data acquisition was initiated by an external trigger from the laser controller. The time resolution of the registered laser pulse was obtained from the standard deviation of the time delta between the trigger signal and the detector signal. As this value still includes the time uncertainty of the trigger signal, the actual detector time resolution was calculated as:

$$\begin{aligned}\sigma_{\Delta t} &= \sqrt{\sigma_{\text{det}}^2 + \sigma_{\text{trg}}^2} \\ \Rightarrow \sigma_{\text{det}} &= \sqrt{\sigma_{\Delta t}^2 - \sigma_{\text{trg}}^2},\end{aligned}\tag{3.9}$$

with  $\sigma_{\text{trg}}$  the time resolution of the trigger signal.  $\sigma_{\text{trg}}$  was determined to be  $<3$  ps. The laser light was injected at the edge of the pad of the sensor, where there is a small gap in the metallization between the pad and the charge collection ring. The data acquisition setup using the UCSCSingleChannel amplifier and R&S RTP164 oscilloscope was used in this experiment.

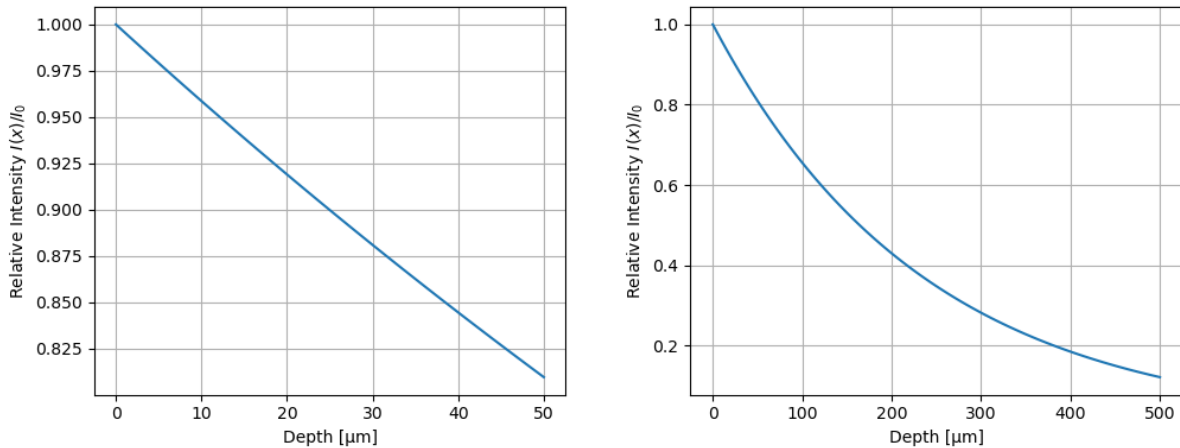


**Figure 3.12:** 370 nm laser light intensity loss inside 4H SiC. The absorption coefficient was estimated at  $42.25 \text{ cm}^{-1}$  from [37].

### Allpix Simulation

**Deposition** To replicate the charge deposition of the UV-Laser, the `DepositionPointCharge` module with `source_type='mip'` was used. This simplification was made, as the used laser loses only about 19.04% of its intensity over the  $50 \mu\text{m}$  of traversed silicon carbide. This behavior is illustrated in figure 3.12. Different settings of the lasers intensity were modelled by varying the `number_of_charges` parameter.

**Field Information** The TCAD fields from the simulation of the edge region of the sensor were applied to the detector via the `ElectricFieldReader`, `WeightingPotentialReader` and `DopingProfileReader`, and the `position` parameter of the `DepositionPointCharge` module was adjusted to generate the charges at the gap in the metallization. As these TCAD fields have a size of only  $256 \mu\text{m}$  in the  $y$  dimension as described in section 3.5, the `size` parameter in 1 was adjusted to `size = 256um`  $256 \mu\text{m}$  in all instances. Comparison simulations using the ideal linear electric field and pad weighting field provided AllPix<sup>2</sup> was also run. The `DopingProfileReader` module was loaded with the TCAD information in all instances.

**Propagation** Simulations using both the `GenericPropagation` and `TransientPropagation` were run for comparison of the resulting data of both modules. The `integration_time` was capped at  $5 \text{ ns}$  and a `charge_per_step` of 100 was used. The `PulseTransfer` parameter `max_depth_distance` was set to  $1 \mu\text{m}$ . The `timestep` and `timestep_max` parameter of the propagation modules was set to  $0.025 \text{ ns}$ , to emulate the  $40 \text{ GS s}^{-1}$  sampling rate of the oscilloscope. The readout electronics were mimicked by the `CSADigitizer` modules using the configuration in configuration 5. Using the `custom` model, the `fit` function and parameter in 3.7 and 3.8 can be set as the `response_function` and `response_parameters`.

Depending on the configured propagation module and field information, the simulations will be referred to as Transient-TCAD, Transient-Linear, Generic-TCAD and Generic-Linear henceforth.

```

1 [CSADigitizer]
2 integration_time = 20ns
3 model = "custom"
4 response_function = "[0] / (TMath::Sqrt (x*x * [1]*[1] + 1) * TMath::
   Sqrt (x*x * [2]*[2] + 1))"
5 response_parameters = [389.0542885897981V*s/C, 2.593747950028592ns
   , 2.593747950028592ns]
6 sigma_noise = 0V

```

**Configuration 5:** Configuration of the CSADigitizer module

### 3.7.2. Proton Experiments

#### Experiment Setup

The SiC diode was tested at the medical treatment and research facility MedAustron in Wiener Neustadt. The facility houses a synchrotron with a circumference of 77 m, capable of accelerating protons up to 800 MeV [38]. The sensor was tested with 62.4 MeV protons. To avoid the occurrence of pile up events, the *low flux* setting [39] of the particle accelerator was used. Readout was performed by the Cividec CSA and R&S RTO6 setup. These readout electronics were not directly mimicked in AllPix<sup>2</sup>, instead the collected charge information was taken from the `PixelCharge` objects in the output file.

#### Allpix Simulation

**Deposition** The proton beam was simulated using the `DepositionGeant4` module. The proton beam was defined in a separate file using the `source_type=macro` and `file_name` parameters. This allows for the configuration of the particle source using the general particle source (GPS) of Geant4. The `max_step_length` parameter was reduced to 10nm, to ensure accurate simulation in the thin support layers of the detector. The standard physics list `FTFP_BERT_LIV` was used. The full setup is shown in configuration 6 and 7.

**Field Information** As the proton beam was adjusted to the centre of the diode, the TCAD field of the pad region was applied to the detector model. As this field is very homogeneous in the  $y$  dimension, it was applied to the whole  $3 \times 3$  mm pad of the sensor. Comparison simulations using the linear electric field and pad weighting potential were again made.

**Propagation** The propagation setups were identical to those explained in section 3.7.1.

```

1 [DepositionGeant4]
2 physics_list = FTFP_BERT_LIV
3 source_type = "macro"
4 file_name = "source_proton.mac"
5 source_position = 0mm 0um 0mm
6 number_of_particles = 1
7 max_step_length = 10nm

```

**Configuration 6:** Configuration of the DepositionGenat4 module to simulate the proton beam and alpha source. The `file_name` parameter was changed for the individual particles' macro files.

```

1 /gps/particle proton
2 /gps/pos/type Point
3 /gps/ene/mono 62.4 MeV
4 /gps/ang/type iso
5 /gps/ang/mintheta 00 deg
6 /gps/ang/maxtheta 00 deg

```

**Configuration 7:** Geant4 GPS macro file to simulate the proton beam.

### 3.7.3. Alpha Experiments

#### Experiment Setup

The third radiation type that the SiC sensor was tested with was alpha radiation. The used alpha source was an Eckert & Ziegler QCRB25 mixed nuclide source. The mixed source is comprised of  $^{239}\text{Pu}$ ,  $^{241}\text{Am}$  and  $^{244}\text{Cm}$  with the decay energies in table 3.4. The 8 mm wide source was placed above the sensor at a distance of about 5.7 mm. The experiment was performed at ambient air pressure. Readout of the sensor was performed by the UCSC TIA and R&S RTP164 oscilloscope.

Nuclide	Alpha Energy [MeV]	Relative Intensity [%]
$^{239}\text{Pu}$	5.1055	11.94
	5.1443	17.11
	5.1566	70.77
$^{241}\text{Am}$	5.3880	1.66
	5.4428	13.10
	5.4856	84.80
$^{244}\text{Cm}$	5.7626	23.10
	5.8048	76.90

**Table 3.4:** Alpha decay energies and relative intensities for the nuclides present in the mixed alpha source [40].

## Allpix Simulation

**Deposition** The `DepositionGeant4` module was employed to simulate a mixed alpha source. Each AllPix<sup>2</sup> event simulates a single primary alpha particle, thus allowing for the individual evaluation of each isotope. When simulating an equal number of events for each nuclide, the events can be combined to assess the entire mixed-alpha source, as the source contains equal activities for each component. The same setup shown in configuration 6 was used with a different GPS macro files for each isotope. The configuration of the <sup>241</sup>Am is shown in configuration 8. As the experiment was conducted in air at ambient pressure, the `world_material` parameter of the `GeometryBuilderGeant4` was set to "air".

**Field Information** The same setup using the pad region TCAD simulation as described in section 3.7.2 was used.

**Propagation** The same propagation module configurations for the `TransientPropagation` and `GenericPropagation` modules were used as in the previously described simulation setups.

```

1 /gps/particle alpha
2 /gps/pos/type Point
3 /gps/ene/type User
4 /gps/hist/type energy
5 /gps/hist/point 5.388 1.66
6 /gps/hist/point 5.443 13.1
7 /gps/hist/point 5.486 84.8
8 /gps/ang/type iso
9 /gps/ang/mintheta 00 deg
10 /gps/ang/maxtheta 00 deg

```

**Configuration 8:** Geant4 GPS macro file to simulate Am241. To simulate the other isotopes, the energy histogram points were changed according to the values in table 3.4.

## 4. Results

### 4.1. UV-Laser Simulations

#### 4.1.1. Charge Collection Efficiency

The resulting CCE for different applied bias voltages was evaluated for the four different simulation configurations (Transient-TCAD, Generic-TCAD, Transient-Linear and Generic-Linear, where the first part refers to the used propagation module and the second part to the used electric field). The CCE versus bias voltage of the TCAD based simulations is shown in figure 4.1 and shows very close agreement between the two propagation modules. This perfect agreement implies the correctness of weighting potential calculated by the process described in section 3.5.1. Figure 4.1 also shows the comparison with the CCE obtained from the measurement. Very close agreement between the simulation and the measurement can be observed. The CCE calculated from the measurement was normalized to 100 % as the maximum measured signal. The CCE obtained from the AllPix<sup>2</sup> output data as  $Q_{\text{col}}/Q_{\text{dep}}$  reaches a maximum of 99.46 % and 99.39 % for the Generic-TCAD and Transient-TCAD simulation respectively. For the Generic-Linear simulation, a peak CCE of 99.60 % was found.

The remaining uncollected charge for the TCAD based simulations is due to the field free space near the implant and buffer layer, which can be seen in figure 3.11. This was confirmed by point-wise deposition of charge in the sensor at specific locations with the `DepositionPointcharge` module in the `point` configuration. The resulting CCE for deposition at different z-locations is shown in figure 4.3. This does however not explain the CCE discrepancy also found for the Generic-Linear simulation setup. It was found, that the `DepositionPointcharge` module in `mip` configuration can actually create some charge carriers outside the sensor, which then get ignored during propagation, depending on the value for the `number_of_steps` parameter. This appears to be a roundoff error in the calculation of the steps.

In contrast to the TCAD based simulations, the Transient-Linear and Generic-Linear simulations show differing results compared to each other, as shown in figure 4.2. This is most likely due to the fact, that the pad weighting potential does not change with the `bias_voltage` parameter of the `ElectricFieldReader`, and is therefore only a viable approximation at or above full depletion, something the AllPix<sup>2</sup> manual does not mention. These simulations both also show different results compared to the measurement, indicating that the linear electric field and pad weighting potential are not a viable approximation for this particular sensor design. This result is expected due to the fact that the used detector's doping profile is not constant across the active volume and therefore strays from an ideal pad detector's setup.

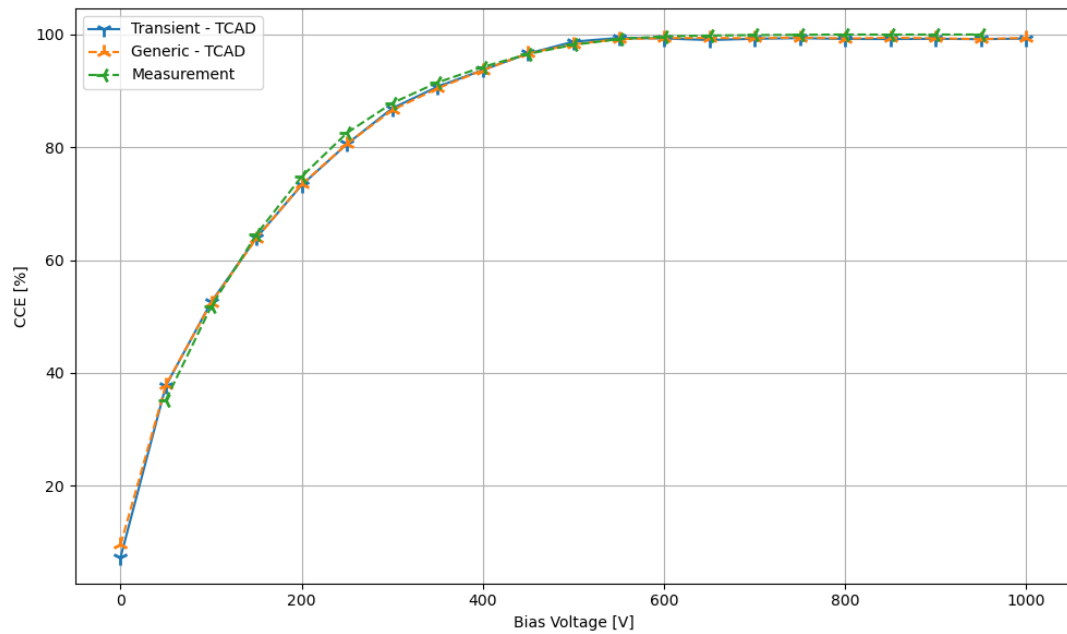


**Figure 4.1:** Comparison of the resulting CCE curves using the Transient-TCAD and Generic-TCAD simulation setups for laser light deposition.

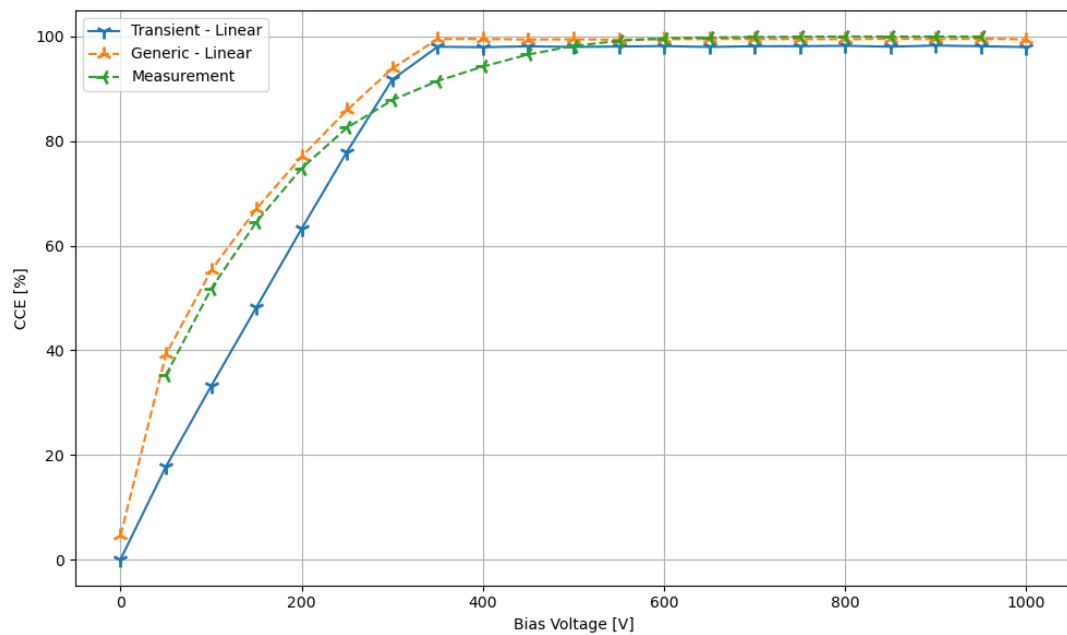


**Figure 4.2:** Comparison of the resulting CCE curves using the Transient-Linear and Generic-Linear simulation setups for laser light deposition.

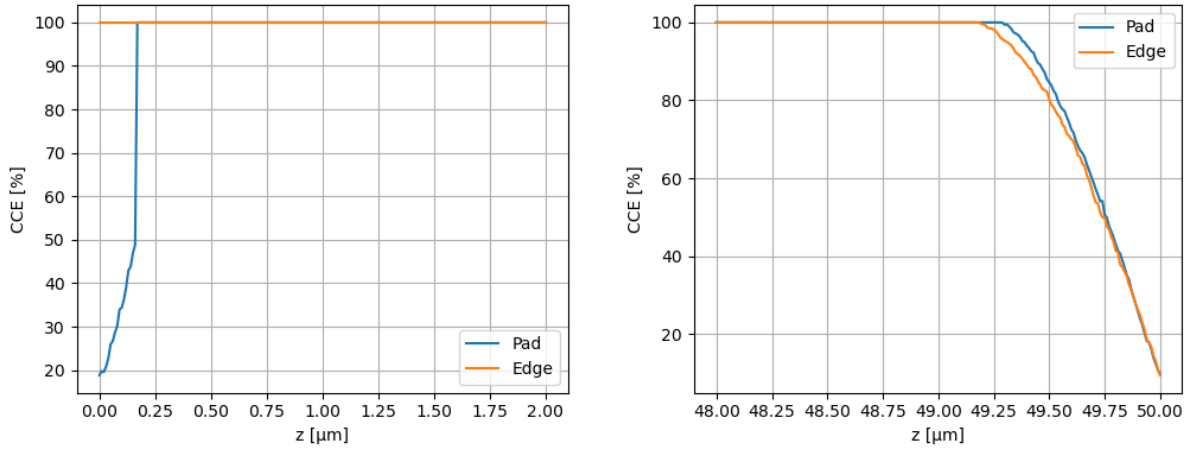


**Figure 4.3:** CCE for pointwise deposition at different depths in the sensor at a bias voltage of 1000 V.

#### 4.1.2. Pulse Shape Comparison

Using the Transient-TCAD simulation setup with the `CSADigitizer` module as described in section 3.7.1, the measured and simulated pulses can be compared. The `number_of_charges` parameter of the `DepositionPointCharge` module was varied until the two signals had an equal peak value. The linear relation of the pulse maximum value to the `number_of_charges` parameter can be seen in figure 4.4. Equal pulse heights were reached at a setting of  $14\,280\ \mu\text{m}^{-1}$ . The resulting pulses are compared in figure 4.5. In this figure, the pulse generated by AllPix<sup>2</sup> appears much narrower than the measured pulse.

By varying the response parameters  $t_1$  and  $t_2$  of the `CSADigitizer` module, a more similar pulse shape could be reached. The best agreement was found at  $t_1 = 1.408\text{ns}$  and  $t_2 = 1.404\text{ns}$ . For this new transfer function, an equal pulse maximum value as the measured signal was reached at a `number_of_charges` setting of  $12\,340\ \mu\text{m}^{-1}$ . The resulting pulse compared to the measured pulse can be seen in figure 4.6. The resulting bode plot using these new response function parameters is shown in figure 4.7. This discrepancy implies that the measured transfer function is incorrect, which can be due to a number of reasons. One possibility is, that the detector's capacitance was not correctly accounted for during the measurement. Another possible explanation are reflections in the measurement setup, which would decrease the observed gain at high frequencies.

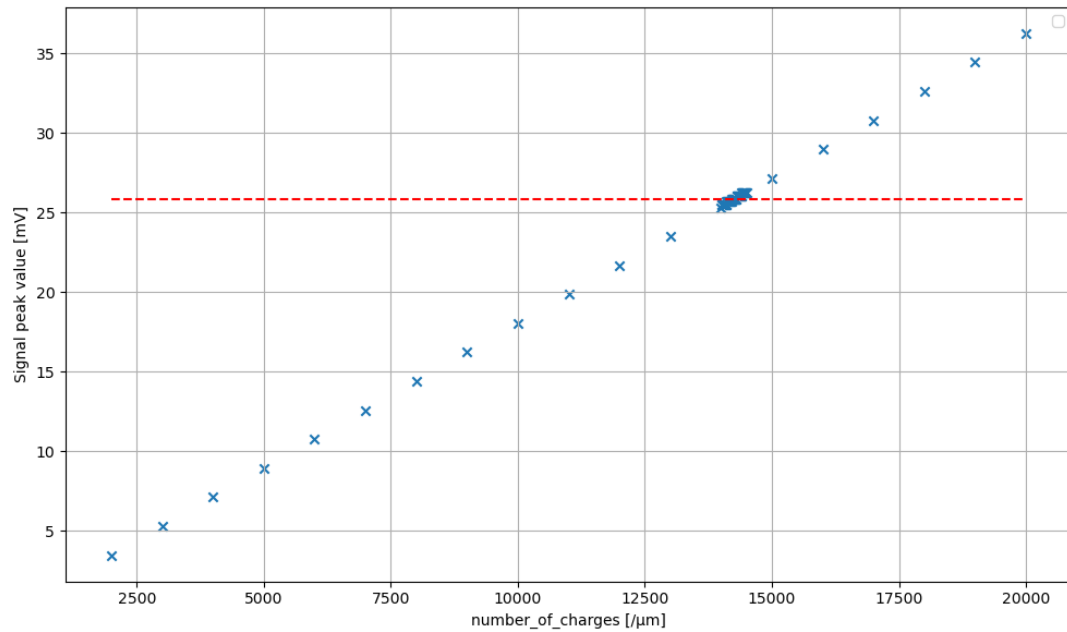


**Figure 4.4:** Pulse peak value versus number\_of\_charges parameter. A linear relation between the two quantities can be seen. The red line indicates the height of the measured pulse.

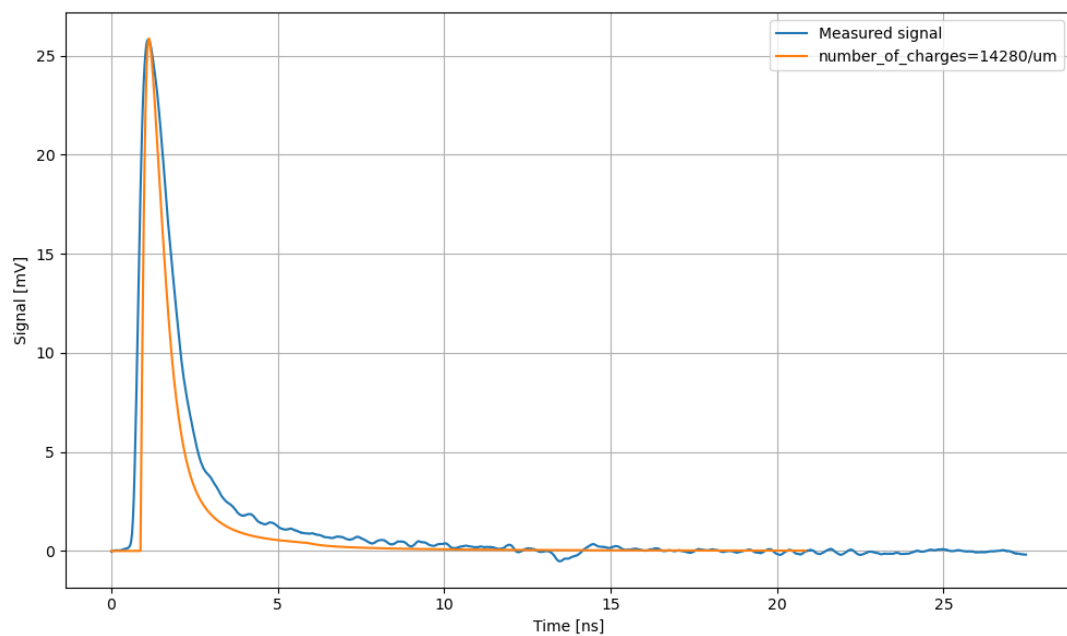


**Figure 4.5:** Comparison of the measured pulse response for irradiation with the UV laser at a bias voltage of 400 V and a pulse generated by a corresponding AllPix<sup>2</sup>simulation with the CSADigitizer settings in configuration 5.

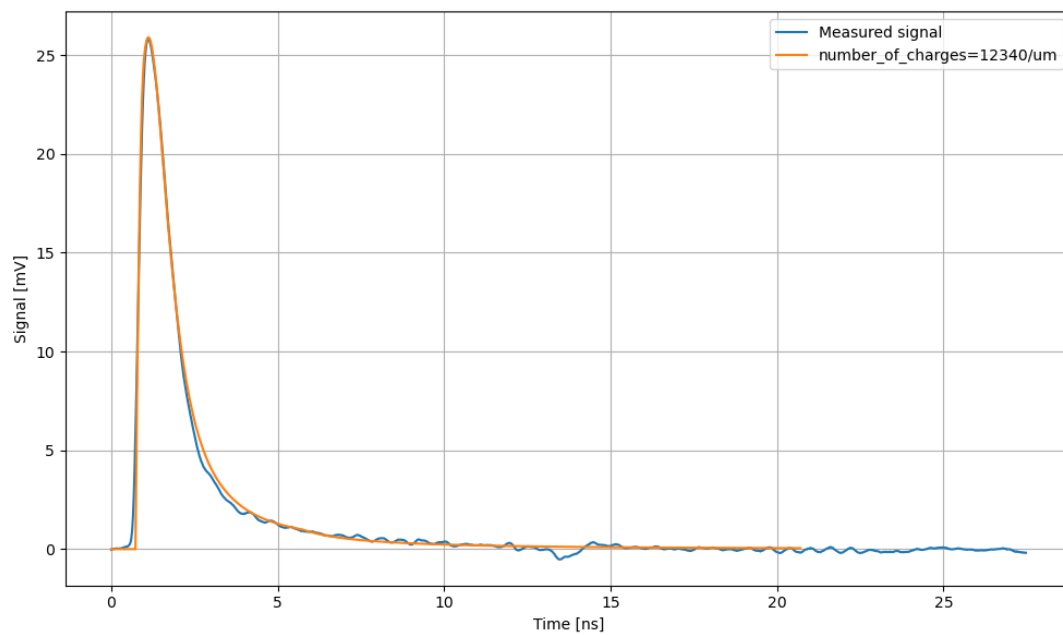


**Figure 4.6:** Comparison of the measured pulse response for irradiation with the UV laser at a bias voltage of 400 V and a pulse generated by a corresponding AllPix<sup>2</sup> simulation with the adjusted CSADigitizer settings.

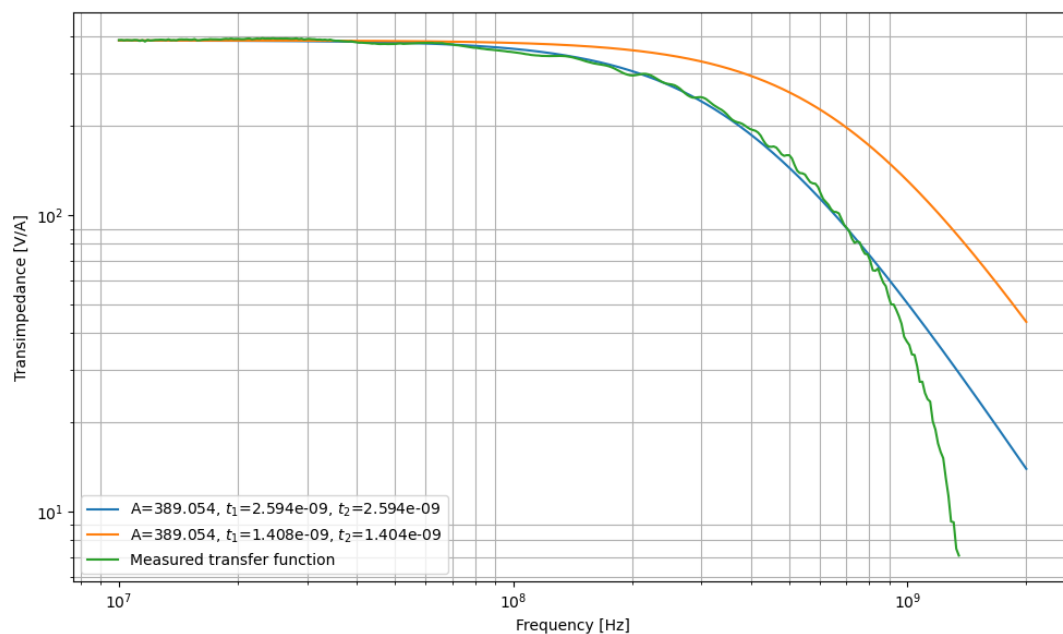


**Figure 4.7:** Bode plot of the adjusted transfer function (orange) compared to the measured function (green) and previous fit (blue).

### 4.1.3. Time Resolution

The time resolution of the detector sample was evaluated at a bias voltage of 400 V according to equation 3.9. Using the pulse analyzer software, a noise RMS of 0.825 mV was determined. This value was used for the pseudo-event generation as explained in 3.6.3. The simulated time resolution was evaluated using both settings of the `CSADigitizer` module from the 'start time' and 'start time interpolated' parameters calculated by the pulse analyzer software, as described in section 3.2.1. The resulting time resolution using the improved response function fit is plotted against the signal-to-noise ratio in figure 4.8. A function of the form  $\sigma_t = \frac{A}{(x-B)} + C$  was fitted to the individual time resolution trends. The resulting fit parameters are listed in table 4.5. In figure 4.8, as expected, the time resolution using the 'start time interpolated' parameter is consistently lower than that using the 'start time'. Both are lower than the measured time resolution, hinting at an unaccounted source of jitter still present in the measurement setup, which poses a lower limit on the time resolution.

The observed time resolutions are quite small, on the order of tens of ps, however, these values have to be taken in consideration of the huge amount of deposited charge at  $\sim 100$  MIPs. These amounts of deposited charge are not feasible to reach in real applications, where instead depositions of 1 MIP to a few tens of MIPs are more realistic. This implies, that the used amplifier is not suitable for the detection of such particles, and instead an amplifier with lower noise and/or lower bandwidth is needed to accurately detect the smaller signals obtained with SiC based detectors. Another option is to increase the signal amplitude, which can be achieved by a low gain avalanche diode (LGAD) [41].

Time Parameter	A	B	C
start time	103.842	6.382	5.574
start time interpolated	90.856	6.882	2.791

**Table 4.5:** Fit parameters for the time resolution trends using the 'start time' or 'start time interpolated' parameter and the initial or improved response function fit.

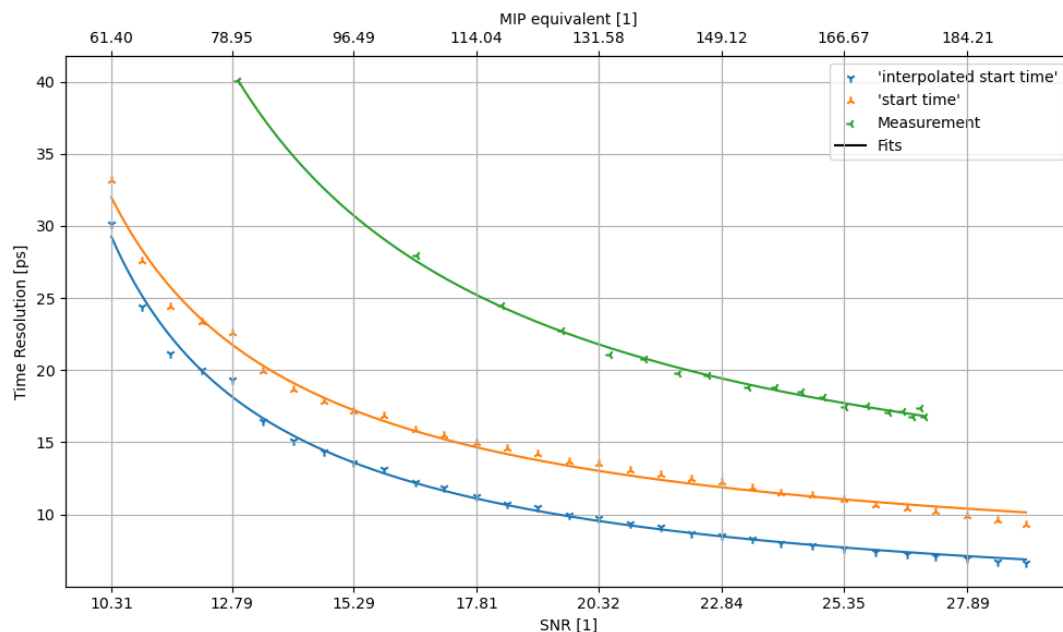
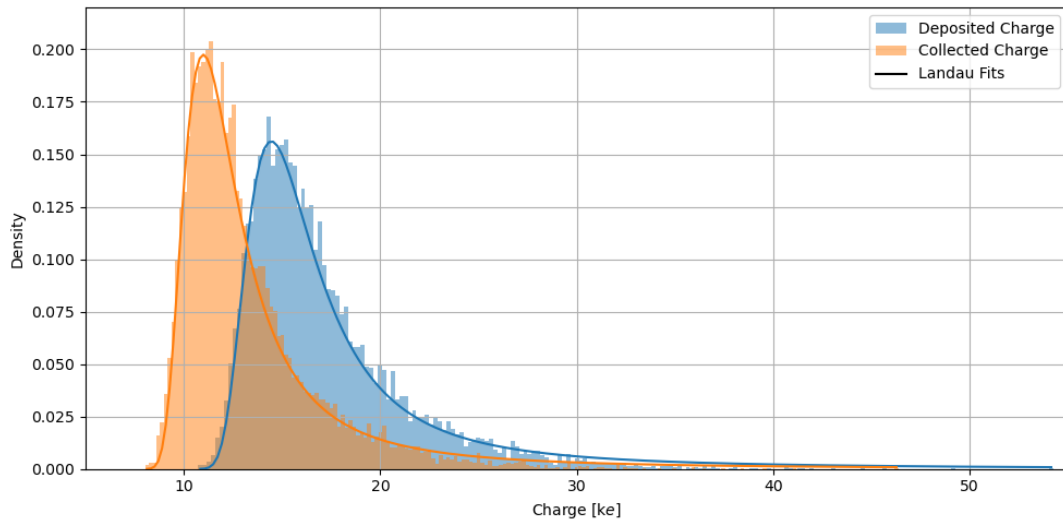


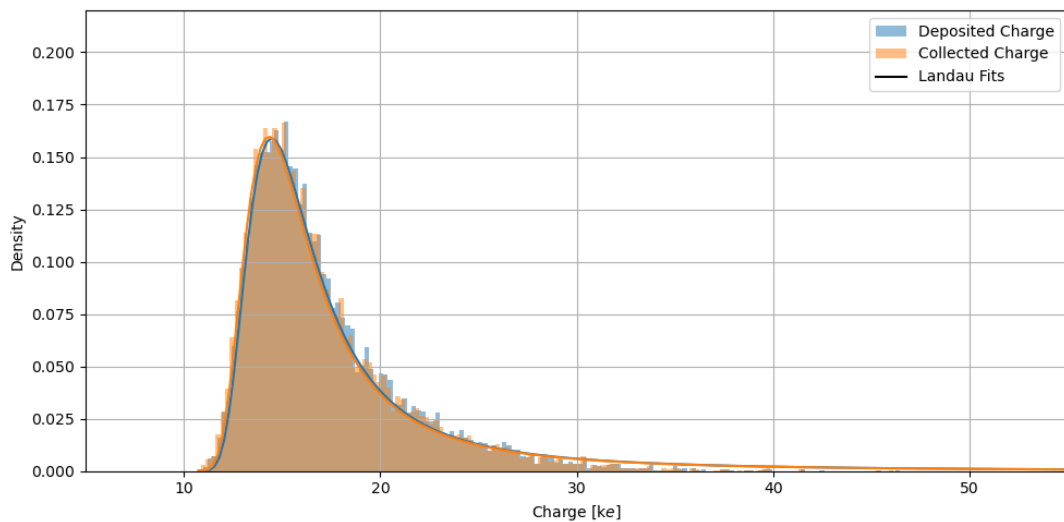
**Figure 4.8:** Observed time resolution using the 'start time' and 'start time interpolated' parameter of the pulse analyzer software and the CSADigitizer settings found in section 4.1.2 compared to the measured time resolution. For reference, the secondary  $x$ -axis shows the MIP equivalent charge deposition.

## 4.2. Proton Simulations

Figure 4.9 shows the histograms and corresponding Landau fits of the deposited and collected charges for two exemplary simulations below (4.9a) and above (4.9b) full depletion of the sensor. All histograms follow a Landau distribution as expected. Below full depletion, the collected charges are shifted towards lower counts compared to the deposited charges. The collected charge histogram should follow the Landau distribution that would be obtained from a fully depleted detector with a thickness of the size of the depletion zone of the under-depleted detector, which is a Landau distribution with smaller most probable value and width. The fit parameters were found at  $MPV = 14.45$  and  $\sigma = 1.16$  for the deposited charge, and  $MPV = 10.98$  and  $\sigma = 0.91$  for the collected charge histogram. Above full depletion, more or less all deposited charges are also collected, and the two histograms coincide almost perfectly. The most probable values for the Landau fits to the histograms are 14.46 and 14.33 for the deposited and collected charge histograms respectively, indicating only a small amount of uncollected charge.



(a) Deposited and collected charges at a bias voltage of 200 V.



(b) Deposited and collected charges at a bias voltage of 600 V.

**Figure 4.9:** Histograms and corresponding Landau fits of the deposited and collected charges for a 62.4 MeV proton beam for applied bias voltages below and above full depletion using the Generic-TCAD simulation setup.

#### 4.2.1. Charge Collection Efficiency

Figure 4.10 shows a comparison of the CCE versus bias voltage for the Generic-TCAD and Generic-Linear simulations to the experimentally obtained CCE for 62.4 MeV protons. Peak CCEs of 99.25 % and 99.11 % for the Generic-TCAD and Transient-TCAD (not shown) simulation respectively. For the Generic-Linear simulation, a peak CCE of 100 % was found. The comparison of the TCAD based simulation to the measurement, again, shows good agreement, while the linear field based simulation strays quite strongly from the measurement.

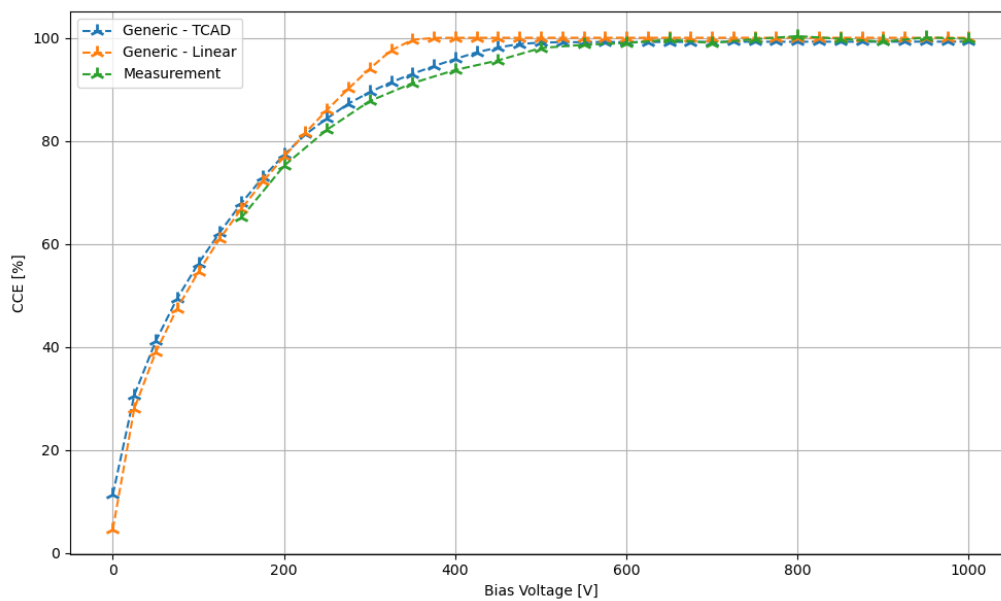


**Figure 4.10:** Comparison of the experimentally measured CCE to the resulting CCE curves using the Generic-TCAD and Generic-Linear simulation setups for a 62.4 MeV proton beam at different sensor bias voltages.

### 4.3. Alpha Simulations

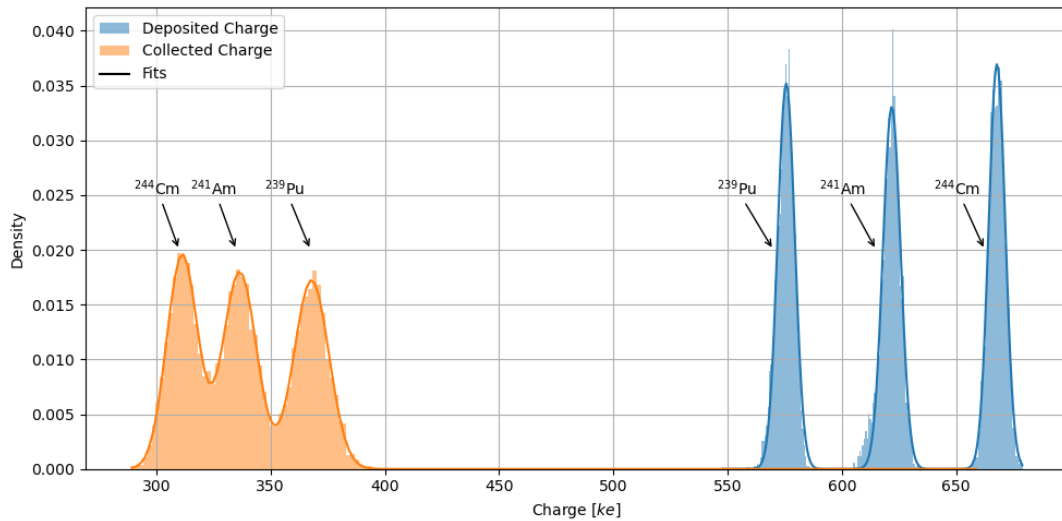
Figure 4.11 shows histograms of the number of deposited and collected charges for applied bias voltages of 6 V (4.11a) and 100 V (4.11b) using the Generic-TCAD setup in vacuum. The sum of the individual Gaussian fits for each isotope are also shown for each histogram. As expected, due to the energy deposition behaviour of charged particles, below sufficient depletion for full charge collection, the lower energy nuclides collected charge is higher, while at sufficient depletion, the higher energy nuclides collected charge is higher. The histograms in figure 4.11b show a small offset of similar magnitude as the previously observed discrepancies. This behaviour is also shown by the Gaussian fit parameters in table 4.6.

#### 4.3.1. Charge Collection Efficiency

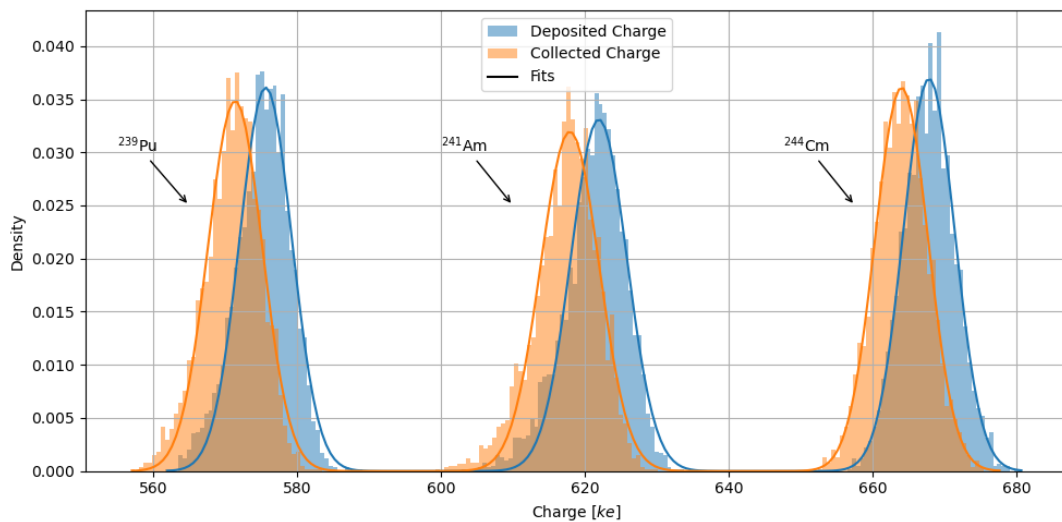
The CCE versus applied bias voltage for the TCAD based simulations is shown in figure 4.12. To provide the same comparison as the previous sections, the CCE obtained with the Generic-Linear simulation setup is shown alongside. For the individual isotopes in the mixed alpha source, the different voltages at which their CCE maximum is reached, can be observed in correspondence to the isotope's different alpha primary energy and associated penetration depths. Also visible is the worse agreement with the measurement as the previous radiation types. At these low applied bias voltages, the detector exhibits a higher capacitance, which, in turn, increases the noise. This effect could explain the worse CCE agreement. The combined CCE for the Generic-TCAD simulation reached a maximum of 99.45 %. For the Generic-Linear simulation a peak of 100 % was reached.

Fitted Histogram	<sup>239</sup> Pu		<sup>241</sup> Am		<sup>244</sup> Cm		Bias Voltage [V]
	$\mu$	$\sigma$	$\mu$	$\sigma$	$\mu$	$\sigma$	
Deposited Charge	647.53	2.31	690.24	2.86	732.82	2.64	20
Collected Charge	581.34	9.16	533.81	11.14	488.32	9.60	
Deposited Charge	647.61	2.10	690.28	2.68	732.81	2.72	100
Collected Charge	643.63	2.36	686.53	2.80	729.22	2.80	

**Table 4.6:** Parameters for fits of Gaussian to individual charge histograms for each isotope and bias voltage.



(a) Deposited and collected charges at a bias voltage of 6 V.



(b) Deposited and collected charges at a bias voltage of 100 V.

**Figure 4.11:** Histograms of the deposited and collected charges for the triple alpha source for applied bias voltages below and above the necessary voltage for reaching  $\sim 100\%$  CCE, using the Generic-TCAD simulation setup.

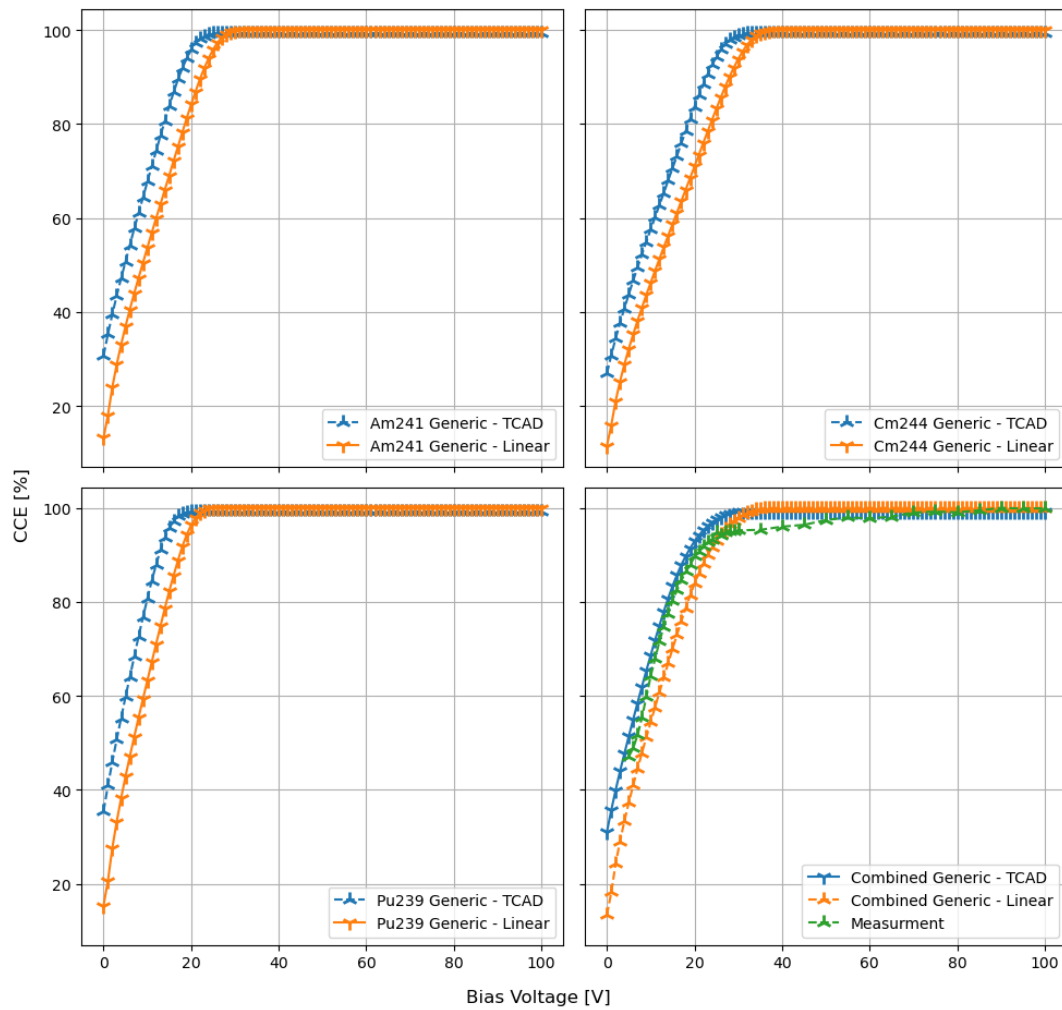


**Figure 4.12:** CCE versus applied bias voltage per nuclide for the Generic-TCAD and Generic-Linear simulations, as well as the mean CCE across all three nuclides compared to the triple alpha source CCE measurements.

## 5. Conclusion

In conclusion, this study helps validate the broader applicability of AllPix<sup>2</sup>, a Monte-Carlo simulation tool which was originally developed with the simulation of conventional silicon based detectors in mind, for the simulation of silicon carbide (SiC) based detectors.

The comprehensive comparison of real-world experiments on a prototype 4H-SiC-based detector with corresponding simulations involved three distinct radiation types, UV-Laser, proton, and alpha particle radiation. As none of the available mobility models in AllPix<sup>2</sup> provide suitable parameters for SiC, a preliminary set of suitable parameters for the Jacoboni Canali model was introduced. The necessary field data was taken from accompanying Synopsys TCAD simulations. A workflow for incorporating said field data in the AllPix<sup>2</sup> simulations was demonstrated.

The quantities looked at in the the comparison included the charge collection efficiency (CCE) and the timing performance. Perfect agreement on the CCE was found not only between the experimental data and the simulation, but also between the two investigated propagation modules, the `GenericPropagation` and `TransientPropagation`, indicating that the in theory less accurate but more efficient `GenericPropagation` is sufficient when evaluating the CCE. Comparisons between the CCE found using the TCAD field data and the idealized fields provided by AllPix<sup>2</sup> itself were made. The results showed, TCAD simulations are essential when working with AllPix<sup>2</sup>, at least given the used detector with its more complex doping concentration profile. However, when evaluating the timing performance, much better values were found for the simulation than the experiment. These discrepancies were attributed to some unaccounted sources of noise present in the experimental setup.

The results of this work show, given correct knowledge of the underlying fields in the detector, AllPix<sup>2</sup> can be a suitable candidate for the simulation of such SiC based detectors. The tool provides a very low barrier of entry with it's exemplary documentation. Configuration is made easy with its `.ini`-like configuration files. However, a closer look at the parameter set used for the propagation, in order to validate and correct it where necessary, could be a candidate for future study.

## Acknowledgements

I am extremely grateful to DI Andreas Gsponer for his ongoing help and support throughout the execution of my master thesis, as well as providing me with the experiment data required for this project.

I also want to thank DI Philipp Gaggl for providing the field data of his TCAD simulations, and even running some additional simulations for me personally, without which this project would not have been possible.

Furthermore, I also want to express my gratitude towards everyone in the HiBPM project team at the institute of high energy physics and DI Dr.techn. Thomas Bergauer personally, for providing a knowledgeable and supporting setting in which to conduct my research, and even making it possible for me to attend the 4th annual AllPix<sup>2</sup> user workshop at the DESY in Hamburg.

Lastly, I would like to thank Assistant Prof. DI Dr.techn. Albert Hirtl for providing the official framework necessary to be able to conduct my master thesis.

## References

- [1] J. Rabkowski, D. Peftitsis, and H.-P. Nee. “Silicon Carbide Power Transistors: A New Era in Power Electronics Is Initiated”. In: *IEEE Industrial Electronics Magazine* 6 (2012), pp. 17–26. DOI: 10.1109/MIE.2012.2193291.
- [2] A. K. Agarwal. “An overview of SiC power devices”. In: *2010 International Conference on Power, Control and Embedded Systems*. 2010, pp. 1–4. DOI: 10.1109/ICPCES.2010.5698670.
- [3] G. Moliere. “Theorie der streuung schneller geladener teilchen ii mehrfach-und vielfachstreuung”. In: *Zeitschrift für Naturforschung A* 3 (1948), pp. 78–97.
- [4] R. L. Workman et al. “Review of Particle Physics”. In: *Progress of Theoretical and Experimental Physics* 2022 (2022). 083C01. DOI: 10.1093/ptep/ptac097. eprint: <https://academic.oup.com/ptep/article-pdf/2022/8/083C01/49175539/ptac097.pdf>.
- [5] P. Cirrone et al. “A 62MeV proton beam for the treatment of ocular melanoma at Laboratori Nazionali del Sud-INFN”. In: *Nuclear Science, IEEE Transactions on* 51 (2004), pp. 860–865. DOI: 10.1109/TNS.2004.829535.
- [6] P. V. Vavilov. “IONIZATION LOSSES OF HIGH-ENERGY HEAVY PARTICLES”. In: *Soviet Phys. JETP* Vol: 5 (1957).
- [7] H. Kolanoski and N. Wermes. *Teilchendetektoren: Grundlagen und Anwendungen*. Springer, 2016. DOI: 10.1007/978-3-662-45350-6.
- [8] I. Henins. “Precision Density Measurement of Silicon”. In: *Journal of Research of the National Bureau of Standards. Section A, Physics and Chemistry* 68A (5 1964), p. 529. DOI: 10.6028/JRES.068A.050.
- [9] S. Ramo. “Currents Induced by Electron Motion”. In: *Proceedings of the IRE* 27 (1939), pp. 584–585. DOI: 10.1109/JRPROC.1939.228757.
- [10] W. Shockley. “Currents to Conductors Induced by a Moving Point Charge”. In: *Journal of Applied Physics* 9 (2004), pp. 635–636. DOI: 10.1063/1.1710367. eprint: [https://pubs.aip.org/aip/jap/article-pdf/9/10/635/8059000/635\\_1\\_online.pdf](https://pubs.aip.org/aip/jap/article-pdf/9/10/635/8059000/635_1_online.pdf).
- [11] M. Ferrero et al. *An Introduction to Ultra-Fast Silicon Detectors: Design, Tests, and Performances*. 2021. DOI: 10.1201/9781003131946.
- [12] “Physical Properties of Silicon Carbide”. In: *Fundamentals of Silicon Carbide Technology*. John Wiley & Sons, Ltd, 2014. Chap. 2, pp. 11–38. DOI: <https://doi.org/10.1002/9781118313534.ch2>. eprint: <https://onlinelibrary.wiley.com/doi/pdf/10.1002/9781118313534.ch2>.
- [13] P. Barletta et al. *Fast Timing With Silicon Carbide Low Gain Avalanche Detectors*. 2022. arXiv: 2203.08554 [physics.ins-det].

- [14] T. Kimoto. “2 - SiC material properties”. In: *Wide Bandgap Semiconductor Power Devices*. Ed. by B. J. Baliga. Woodhead Publishing Series in Electronic and Optical Materials. Woodhead Publishing, 2019, pp. 21–42. DOI: <https://doi.org/10.1016/B978-0-08-102306-8.00002-2>.
- [15] M. De Napoli. “SiC detectors: A review on the use of silicon carbide as radiation detection material”. In: *Frontiers in Physics* (2022), p. 769. DOI: <https://doi.org/10.3389/fphy.2022.898833>.
- [16] *Allpix Squared - Website*. <https://allpix-squared.docs.cern.ch/>. Date accessed: 11.07.2023.
- [17] S. Agostinelli et al. “Geant4—a simulation toolkit”. In: *Nuclear Instruments and Methods in Physics Research Section A: Accelerators, Spectrometers, Detectors and Associated Equipment* 506 (3 2003), pp. 250–303. DOI: 10.1016/S0168-9002(03)01368-8.
- [18] R. Brun and F. Rademakers. “ROOT — An object oriented data analysis framework”. In: *Nuclear Instruments and Methods in Physics Research Section A: Accelerators, Spectrometers, Detectors and Associated Equipment* 389 (1997). New Computing Techniques in Physics Research V, pp. 81–86. DOI: [https://doi.org/10.1016/S0168-9002\(97\)00048-X](https://doi.org/10.1016/S0168-9002(97)00048-X).
- [19] S. Spannagel et al. “Allpix<sup>2</sup>: A Modular Simulation Framework for Silicon Detectors”. In: *Nucl. Instrum. Methods Phys. Res. A* 901 (2018), pp. 164–172. DOI: 10.1016/j.nima.2018.06.020. arXiv: 1806.05813.
- [20] W. Riegler and G. Aglieri Rinella. “Point charge potential and weighting field of a pixel or pad in a plane condenser”. In: *Nuclear Instruments and Methods in Physics Research Section A: Accelerators, Spectrometers, Detectors and Associated Equipment* 767 (2014), pp. 267–270. DOI: <https://doi.org/10.1016/j.nima.2014.08.044>.
- [21] G. Masetti, M. Severi, and S. Solmi. “Modeling of carrier mobility against carrier concentration in arsenic-, phosphorus-, and boron-doped silicon”. In: *IEEE Transactions on Electron Devices* 30 (1983), pp. 764–769. DOI: 10.1109/T-ED.1983.21207.
- [22] C. Canali et al. “Electron and hole drift velocity measurements in silicon and their empirical relation to electric field and temperature”. In: *IEEE Transactions on Electron Devices* 22 (1975), pp. 1045–1047. DOI: 10.1109/T-ED.1975.18267.
- [23] D. Stefanakis and K. Zekentes. “TCAD models of the temperature and doping dependence of the bandgap and low field carrier mobility in 4H-SiC”. In: *Microelectronic Engineering* 116 (2014), pp. 65–71. DOI: <https://doi.org/10.1016/j.mee.2013.10.002>.
- [24] T. Hatakeyama et al. “Measurement of Hall Mobility in 4H-SiC for Improvement of the Accuracy of the Mobility Model in Device Simulation”. In: *Materials Science Forum - MATER SCI FORUM* 433-436 (2003), pp. 443–446. DOI: 10.4028/www.scientific.net/MSF.433-436.443.

- [25] T. Ayalew. “SiC semiconductor devices technology, modeling and simulation”. PhD thesis. 2004. DOI: <https://doi.org/10.34726/hss.2004.04281063>.
- [26] H.-E. Nilsson, U. Sannemo, and C. S. Petersson. “Monte Carlo simulation of electron transport in 4H-SiC using a two-band model with multiple minima”. In: *Journal of Applied Physics* 80 (1996), pp. 3365–3369. DOI: 10.1063/1.363249. eprint: [https://pubs.aip.org/aip/jap/article-pdf/80/6/3365/8052126/3365\\\_1\\\_online.pdf](https://pubs.aip.org/aip/jap/article-pdf/80/6/3365/8052126/3365\_1\_online.pdf).
- [27] *RS DRS4 Run Analysis*. [https://gitlab.com/dd-hephy/HiBPM/RS\\_DRS4\\_run\\_analysis](https://gitlab.com/dd-hephy/HiBPM/RS_DRS4_run_analysis). Date accessed: 22.08.2023.
- [28] *IMB CNM CSIC - Website*. <https://www.imb-cnm.csic.es/>. Date accessed: 14.09.2023.
- [29] W. Haynes. *CRC Handbook of Chemistry and Physics*. CRC Handbook of Chemistry and Physics. CRC Press, 2011.
- [30] Andreas Gsponer. “Neutron Radiation induced Effects in 4H-SiC PiN Diodes”. 24th International Workshop on Radiation Imaging Detectors. Oslo, Norway, 2022.
- [31] *UCSC Single Channel*. <https://twiki.cern.ch/twiki/bin/view/Main/UcscSingleChannel>. Date accessed: 24.09.2023.
- [32] N. Cartiglia et al. “Beam test results of a 16ps timing system based on ultra-fast silicon detectors”. In: *Nuclear Instruments and Methods in Physics Research Section A: Accelerators, Spectrometers, Detectors and Associated Equipment* 850 (2017), pp. 83–88. DOI: <https://doi.org/10.1016/j.nima.2017.01.021>.
- [33] *Cividec Cx-L*. <https://cividec.at/electronics-Cx-L.html>. Date accessed: 10.11.2023.
- [34] *Synopsys Technologies - Website*. <https://www.synopsys.com/>. Date accessed: 06.11.2023.
- [35] *HTCondor - Website*. <https://htcondor.org/>. Date accessed: 06.11.2023.
- [36] *PILAS – picosecond pulsed diode lasers*. <https://www.nktphotonics.com/products/pulsed-diode-lasers/pilas/>. Date accessed: 23.09.2023.
- [37] S. G. Sridhara, R. P. Devaty, and W. J. Choyke. “Absorption coefficient of 4H silicon carbide from 3900 to 3250 Å”. In: *Journal of Applied Physics* 84 (1998), pp. 2963–2964. DOI: 10.1063/1.368403.
- [38] M. Benedikt and A. Wrulich. “MedAustron—Project overview and status”. In: *The European Physical Journal Plus* 126 (2011), pp. 1–11.
- [39] F. Ulrich-Pur et al. “Commissioning of low particle flux for proton beams at MedAustron”. In: *Nuclear Instruments and Methods in Physics Research Section A: Accelerators, Spectrometers, Detectors and Associated Equipment* 1010 (2021), p. 165570. DOI: <https://doi.org/10.1016/j.nima.2021.165570>.

- [40] *National Nuclear Data Center, information extracted from the NuDat database.* <https://www.nndc.bnl.gov/nudat/>. Date accessed: 02.10.2023.
- [41] N. Moffat et al. “Low Gain Avalanche Detectors (LGAD) for particle physics and synchrotron applications”. In: *Journal of Instrumentation* 13 (2018), p. C03014. DOI: 10.1088/1748-0221/13/03/C03014.

## List of Tables

2.1.	Bethe-Bloch equation parameters. . . . .	9
2.2.	Comparison between Si and SiC properties [12–15]. c-axis refers to the stacking orientation. . . . .	18
3.3.	Used parameters for the Masetti Canali model. Since the mobility is anisotropic, two values are given for the relevant parameters where available. The first value represents perpendicular, the second movement parallel to the c-axis. Temperature dependence was neglected and the parameters are therefore only valid at 300 K. The values were taken from [12, 23–25]. The anisotropy was calculated using the factor found in [26]. . . . .	22
3.4.	Alpha decay energies and relative intensities for the nuclides present in the mixed alpha source [40]. . . . .	39
4.5.	Fit parameters for the time resolution trends using the 'start time' or 'start time interpolated' parameter and the initial or improved response function fit. . . . .	46
4.6.	Parameters for fits of Gaussian to individual charge histograms for each isotope and bias voltage. . . . .	50

## List of Figures

2.1.	Bethe-Bloch equation for a number of different materials. [4] . . . . .	9
2.2.	Bragg peak exhibited by 62 MeV protons in water [5]. . . . .	9
2.3.	Comparison between the symmetric Gauss distribution and the asymmetric Landau and Langau distributions. . . . .	10
2.4.	Schematic representation of the band structure for conductors, semiconductors and insulators. Adapted from [7] . . . . .	13
2.5.	On the uncertainty arising from jitter. Adapted from [11]. . . . .	16
2.6.	Time walk stemming from signals with different peak values. Adapted from [11]. . . . .	17
3.1.	Structure of the AllPix <sup>2</sup> framework with the framework core and individual modules. The passing of detector configuration information is indicated by the grey dashed arrows. The red arrows represent the interaction of the modules via the messaging system. Logging information is passed back along the blue dashed arrows. Adapted from [19]. . . . .	19
3.2.	Setup of an Allpix2 simulation using a single detector, where every block represents a single module instantiation. After the geometry construction and field setup, charge carriers are deposited, propagated and collected at the implants. Finally, the resulting signal is digitised and the results are stored. Adapted from [19]. . . . .	20
3.3.	Visualization of the low field mobility versus doping concentration, and the high field mobility and resulting velocities at a fixed doping concentration for electrons and holes. . . . .	23
3.4.	Linegraph of the charge carriers created by an alpha particle hitting an idealized sensor (linear E-field) at an angle. The electrons are colored in blue, the holes in orange. . . . .	24
3.5.	Screenshot of an analyzed waveform in the GUI of the Pulse Analyzer software. . . . .	26
3.6.	Schematic cross section of the detector in use in the experiments [30]. . . . .	27
3.7.	Measured bode plot of the UCSCSingleChannel (orange) and best fit of function 3.7 to the measured data (blue). . . . .	29
3.8.	(Absolute) doping concentration of the TCAD simulated area at the edge of the pad region. . . . .	32
3.9.	Electric field of the TCAD simulation at the edge of the pad region with a bias voltage of 400 V. . . . .	33
3.10.	Weighting potential calculated from the electrostatic potential of the TCAD simulation at the edge of the pad region with a bias voltage of 400 V. . . . .	33
3.11.	Comparison between the analytical linear field for a full depletion voltage of 350 V available in AllPix <sup>2</sup> and the simulated TCAD field at different applied bias voltages. . . . .	34

3.12.	370 nm laser light intensity loss inside 4H SiC. The absorption coefficient was estimated at $42.25 \text{ cm}^{-1}$ from [37]. . . . .	37
4.1.	Comparison of the resulting CCE curves using the Transient-TCAD and Generic-TCAD simulation setups for laser light deposition. . . . .	42
4.2.	Comparison of the resulting CCE curves using the Transient-Linear and Generic-Linear simulation setups for laser light deposition. . . . .	42
4.3.	CCE for pointwise deposition at different depths in the sensor at a bias voltage of 1000 V. . . . .	43
4.4.	Pulse peak value versus <code>number_of_charges</code> parameter. A linear relation between the two quantities can be seen. The red line indicates the height of the measured pulse. . . . .	44
4.5.	Comparison of the measured pulse response for irradiation with the UV laser at a bias voltage of 400 V and a pulse generated by a corresponding AllPix <sup>2</sup> simulation with the CSADigitizer settings in configuration 5. . . .	44
4.6.	Comparison of the measured pulse response for irradiation with the UV laser at a bias voltage of 400 V and a pulse generated by a corresponding AllPix <sup>2</sup> simulation with the adjusted CSADigitizer settings. . . . .	45
4.7.	Bode plot of the adjusted transfer function (orange) compared to the measured function (green) and previous fit (blue). . . . .	45
4.8.	Observed time resolution using the 'start time' and 'start time interpolated' parameter of the pulse analyzer software and the CSADigitizer settings found in section 4.1.2 compared to the measured time resolution. For reference, the secondary <i>x</i> -axis shows the MIP equivalent charge deposition. .	47
4.9.	Histograms and corresponding Landau fits of the deposited and collected charges for a 62.4 MeV proton beam for applied bias voltages below and above full depletion using the Generic-TCAD simulation setup. . . . .	48
4.10.	Comparison of the experimentally measured CCE to the resulting CCE curves using the Generic-TCAD and Generic-Linear simulation setups for a 62.4 MeV proton beam at different sensor bias voltages. . . . .	49
4.11.	Histograms of the deposited and collected charges for the triple alpha source for applied bias voltages below and above the necessary voltage for reaching $\sim 100\%$ CCE, using the Generic-TCAD simulation setup. . . . .	51
4.12.	CCE versus applied bias voltage per nuclide for the Generic-TCAD and Generic-Linear simulations, as well as the mean CCE across all three nuclides compared to the triple alpha source CCE measurements. . . . .	52

## A. Appendix

### A.1. Configuration of the Transient-TCAD UV-Laser Simulation

The following configurations showcase the full setup that was used for the Transient-TCAD simulations of the UV-Laser. The entry-point is the HTCondor submit-file `photon_cce_transient_tcad.sub` shown in 9. The scan over the applied bias voltage is realized by inserting the requested voltage in the file name of the applied TCAD fields. This of course requires the files to be named accordingly.

```

1 # Before run:
2 # Check that scratch directory exists, with sub-directory "log"
3 initialdir = /scratch/psommerer/allpix/photon/CCE/TRANSIENT/TCAD
4 tcaddir = /home/users/psommerer/TCAD_FIELDS/simple_cut
5
6 universe = docker
7 docker_image = registry.gitlab.com/dd-hephy/hibpm/allpix-squared-fork:
  dev
8
9 executable = ./job_photon_cce_transient_tcad.sh
10 arguments = "$(filename) -o workers=$(request_cpus) -o multithreading=
  false -o number_of_events=$(number_of_events) -o
  DepositionPointCharge.number_of_charges=$INT(e)/um -o
  ElectricFieldReader.file_name=Efield_simpleCNM_guard0_$INT(v)
  V_des_ElectricField.init -o DopingProfileReader.file_name=
  Efield_simpleCNM_guard0_$INT(v)V_des_DopingConcentration.init -o
  WeightingPotentialReader.file_name=Efield_simpleCNM_guard0_$INT(v)
  V_des_WeightingField.init"
11
12 # Directory containing allpix conf files
13 allpix_dir = /home/users/psommerer/allpix-squared-sic/photon/CCE/
  TRANSIENT/TCAD/
14 # Transfer allpix files
15 # Use absolute paths, because the initialdir is set on the /scratch
  directory
16 transfer_input_files = $(allpix_dir)detector.conf,$(allpix_dir)geometry.
  conf,$(allpix_dir)simulation.conf,$(tcaddir)/efield/
  Efield_simpleCNM_guard0_$INT(v)V_des_ElectricField.init,$(tcaddir)/
  doping/Efield_simpleCNM_guard0_$INT(v)V_des_DopingConcentration.init,
  $(tcaddir)/weightingField/Efield_simpleCNM_guard0_$INT(v)
  V_des_WeightingField.init
17 should_transfer_files = YES
18 transfer_output_files = output/$(filename)_pulses.root
19
20 when_to_transfer_output = ON_EXIT
21 # Write stdout/stderr directly to correct scratch directory
22 output = log/out_$(filename).$(process)
23 error = log/err_$(filename).$(Process)
24 log = log/log_$(filename).$(Process)
25 request_cpus = 1
26

```

```

27 filename = $INT(v)V_$(INT(e))E
28
29 number_of_events = 10
30
31 min_v = 0
32 max_v = 2000
33 min_e = 12000
34 max_e = 12000
35 step_v = 50
36 step_e = 1000
37
38 steps_v = ((($(max_v) - $(min_v)) / $(step_v))+1)
39 steps_e = ((($(max_e) - $(min_e)) / $(step_e))+1)
40
41 N = ($(steps_v) * $(steps_e))
42
43 I = (($(Process) / $(steps_e))
44 J = (($(Process) % $(steps_e))
45
46 v = ($(min_v)+$(step_v)*$(I))
47 e = ($(min_e)+$(step_e)*$(J))
48
49 queue $INT(N)

```

**Configuration 9:** HTCondor submit-file for the UV-Laser simulation. This configuration allows for simultaneous scanning over the applied bias voltage and the total amount of deposited charge.

```

1 #!/bin/bash
2
3 if [ $# -lt 1 ]; then
4     echo "Usage: $0 file_name allpix_arguments"
5     exit 1
6 fi
7
8 set -e
9
10 echo "${@:2}"
11 allpix -c simulation.conf -o ROOTObjectReader.file_name=output/$1.root -
    o ROOTObjectWriter.file_name=$1_pulses.root ${@:2}

```

**Configuration 10:** Intermittent shell script `job_photon_cce_transient_tcad.sh` to call AllPix<sup>2</sup> with the parameters from HTCondor.

```

1 [AllPix]
2 detectors_file = "geometry.conf"
3 output_directory = "output"
4 model_paths = ./
5 root_file = "plots.root"
6
7 [DepositionPointCharge]
8 source_type = "mip"

```

```

9 model = "fixed"
10 position = 0um -76um
11
12 [ElectricFieldReader]
13 model = "mesh"
14 field_mapping = PIXEL_FULL
15
16 [WeightingPotentialReader]
17 log_level=DEBUG
18 field_mapping = PIXEL_FULL
19 ignore_field_dimensions = true
20 name = "detector"
21 model = "mesh"
22
23 [DopingProfileReader]
24 model = "mesh"
25 field_mapping = PIXEL_FULL
26
27 [TransientPropagation]
28 temperature = 300K
29 integration_time = 5ns
30 charge_per_step = 100
31 timestep = 0.025ns
32 timestep_max = 0.025ns
33 mobility_model = "masetti_canali"
34 propagate_holes = true
35
36 [PulseTransfer]
37 max_depth_distance = 1um
38
39 [CSADigitizer]
40 integration_time = 20ns
41 model = "custom"
42 response_function = "[0] / (TMath::Sqrt (x*x * [1]*[1] + 1) * TMath::
    Sqrt (x*x * [2]*[2] + 1))"
43 response_parameters = [389V*s/C,2.594ns,2.594ns]
44 sigma_noise = 0V
45
46 [ROOTObjectWriter]
47 #exclude = PropagatedCharge

```

**Configuration 11:** simulation.conf for the UV-Laser simulation. The corresponding detector configuration is shown in configuration 1.

```

1 [detector]
2 type = "detector"
3 position = 0um 0um 0um
4 orientation_mode = "xyz"
5 orientation = 0deg 0deg 0deg

```

**Configuration 12:** geometry.conf for the UV-Laser simulation.

## A.2. Python Code for Weighting Field Calculation

```

1 def calc_weighting_field(f0v : str, f1v : str, fout : str, delta_V = 1)
  -> None:
2     """Calculates weighting field by subtracting the electrostatic
   potential in INIT file f1v from f0v, and saving in out
3
4     Args:
5         f0v (str): File path of the first input .INIT file (with smalled
   applied bias voltage)
6         f1v (str): File path of the second input .INIT file (with larger
   applied bias voltage)
7         fout (str): File path of the output .INIT file. Will be
   overwritten if it already exists
8         delta_V (int, optional): Difference in applied bias voltage
   between f0v and f1v. Defaults to 1.
9     """
10
11     file_1V = open(f1v, "r").readlines()
12     file_0V = open(f0v, "r").readlines()
13
14     output_file = open(fout, "w")
15
16     for count, (l0,l1) in enumerate(zip(file_0V, file_1V)):
17         if count in range(5):
18             if l0 != l1:
19                 import warnings
20                 warnings.warn("The provided INIT files headers do not
   match\n\t{}\n\t{}".format(l0,l1))
21                 output_file.write(l0)
22                 continue
23                 x0,y0,z0,v0 = l0.split(" ")
24                 x1,y1,z1,v1 = l1.split(" ")
25                 if x0!=x1 or y0!=y1 or z0!=z1:
26                     raise
27                 vout = (1-(float(v1)-float(v0))/delta_V)
28                 if vout>0.99999:
29                     vout = 0.99999
30                 elif vout<0.00001:
31                     vout = 0.00001
32                 output_file.write("{} {} {} {:.f}\n".format(x0,y0,z0,vout))
33     output_file.close()

```

**Configuration 13:** Python code for the calculation of the weighting field.

### A.3. Python Code for AllPix<sup>2</sup> ROOT File Analysis

```

1 from ROOT import TFile, gSystem
2 import numpy as np
3 gSystem.Load("/home/paul/allpix-squared-fork/install/lib/
  libAllpixModuleROOTObjectWriter.so")
4
5 def getNumberOfCollectedCharges(fileName: str, treeName = "PixelCharge",
  detectorName = "detector"):
6     """Reads the collected charge from the ROOT file
7
8     Args:
9         fileName (str): Filename of the ROOT file to read
10        treeName (str, optional): Name of the ROOT tree containing the
  collected charge information. Defaults to "PixelCharge".
11        detectorName (str, optional): Name of the detector to read.
  Defaults to "detector".
12
13     Returns:
14        numpy.array: Numpy array with the collected charge for each
  event.
15        """
16        file = TFile.Open(fileName)
17        tree = file.Get(treeName)
18        numEvents = tree.GetEntries()
19        charges = np.empty(numEvents)
20        for i in range(numEvents):
21            tree.GetEntry(i)
22            if not len(getattr(tree, detectorName)): charges[i] = 0
23            else: charges[i] = getattr(tree, detectorName)[0].
  getAbsoluteCharge()
24        return charges
25
26 def getNumberOfDepositedCharges(fileName: str, treeName = "
  DepositedCharge", detectorName = "detector", includeHoles = False):
27     """Reads the deposited charge from the ROOT file
28
29     Args:
30        fileName (str): Filename of the ROOT file to read
31        treeName (str, optional): Name of the ROOT tree containing the
  deposited charge information. Defaults to "DepositedCharge".
32        detectorName (str, optional): Name of the detector to read.
  Defaults to "detector".
33        includeHoles (bool, optional): If set to true, two Numpy arrays
  are returned instead of one,
34        one for the amount of electrons and one for the amount of
  holes deposited. Defaults to False.
35
36     Returns:
37        (Tuple of) numpy.array: Numpy array(s) with the deposited charge
  for each event.
38        """

```

```

39 file = TFile.Open(fileName)
40 tree = file.Get(treeName)
41 numEvents = tree.GetEntries()
42 e = np.zeros(numEvents)
43 h = np.zeros(numEvents)
44 for i in range(numEvents):
45     tree.GetEntry(i)
46     for deposit in getattr(tree, detectorName):
47         if deposit.getSign() == -1:
48             e[i] += deposit.getCharge()
49         elif includeHoles:
50             h[i] += deposit.getCharge()
51 if includeHoles:
52     return e, h
53 else:
54     return e
55
56 def getSignal(fileName: str, treeName = "PixelPulse", detectorName = "
57 detector"):
58     """Reads the generated signal from the ROOT file
59
60     Args:
61     fileName (str): Filename of the ROOT file to read
62     treeName (str, optional): Name of the ROOT tree containing the
63     signal information. Defaults to "PixelPulse".
64     detectorName (str, optional): Name of the detector to read.
65     Defaults to "detector".
66
67     Returns:
68     numpy.array: Numpy array with the signal (as numpy.array) for
69     each event.
70     """
71     file = TFile.Open(fileName)
72     tree = file.Get(treeName)
73
74     numEvents = tree.GetEntries()
75     tree.GetEntry(0)
76     try:
77         numTimeSteps = len(getattr(tree, detectorName)[0])
78     except IndexError:
79         numTimeSteps = 0
80     arr = np.empty([numEvents, numTimeSteps])
81     for i in range(numEvents):
82         tree.GetEntry(i)
83         try:
84             pixelPulse = getattr(tree, detectorName)[0]
85             timeSteps = len(pixelPulse)
86             arr[i] = np.frombuffer(pixelPulse.data(), dtype=np.float,
87 count = timeSteps)*1e6
88         except IndexError:
89             arr[i] = np.zeros(numTimeSteps)
90     return arr

```

```

86
87 def getCurrent(fileName: str, treeName = "PixelCharge", detectorName = "
    detector", fixDimensions = True):
88     """Reads the current (before digitization) from the ROOT file
89
90     Args:
91         fileName (str): Filename of the ROOT file to read
92         treeName (str, optional): Name of the ROOT tree containing the
    current information. Defaults to "PixelCharge".
93         detectorName (str, optional): Name of the detector to read.
    Defaults to "detector".
94         fixDimensions (bool, optional): If set to true, the current
    array for each event will be of equal length (padded with 0 to the
    right). Defaults to True.
95
96     Returns:
97         numpy.array or array: Numpy array if fixDimensions == True, else
    array with the current (as numpy.array) for each event.
98     """
99     file = TFile.Open(fileName)
100    tree = file.Get(treeName)
101
102    numEvents = tree.GetEntries()
103    currents = []
104    for i in range(numEvents):
105        tree.GetEntry(i)
106        pixelCharge = getattr(tree, detectorName)[0]
107        currents.append(np.array(list(pixelCharge.getPulse())))
108
109    if fixDimensions:
110        maxLen = max([len(c) for c in currents])
111        currentsFixed = np.zeros((len(currents), maxLen))
112        for i, c in enumerate(currents):
113            currentsFixed[i][:len(c)] = c
114        return currentsFixed
115    return currents

```

**Configuration 14:** Python code for the extraction of relevant data from the ROOT file generated by AllPix<sup>2</sup>. The path to the AllPix<sup>2</sup> installation in line 3 must be replaced accordingly.